







Isabel Wapenhans¹, Victoria M. Fernandes¹ , Conor O'Malley¹ , Nicky White² , and Gareth G. Roberts¹ 

Key Points:

- Wavelet spectral analysis reveals scale-dependence of North American river profile geometries
- At wavelengths >100 km, these geometries are dominated by regional uplift
- At wavelengths <100 km, erodibility becomes emergent

Supporting Information:

Supporting Information may be found in the online version of this article.

Correspondence to:

G. G. Roberts,
gareth.roberts@imperial.ac.uk

Citation:

Wapenhans, I., Fernandes, V. M., O'Malley, C., White, N., & Roberts, G. G. (2021). Scale-dependent contributors to river profile geometry. *Journal of Geophysical Research: Earth Surface*, 126, e2020JF005879. <https://doi.org/10.1029/2020JF005879>

Received 8 SEP 2020
 Accepted 11 MAY 2021

¹Department of Earth Science and Engineering, Imperial College London, London, UK, ²Department of Earth Sciences, Bullard Laboratories, University of Cambridge, Cambridge, UK

Abstract A range of complex hydraulic and geomorphic processes shape terrestrial landscapes. It remains unclear how these processes act to generate observed drainage networks across scales of interest. To address this issue, we transform observed and synthetic longitudinal river profiles into the spectral domain with a view to interrogating the different scales at which fluvial landscapes are generated. North American river profiles are characterized by red noise (i.e., spectral power, $\phi \propto k^{-2}$, where k is wave number) at wavelengths >100 km and pink noise ($\phi \propto k^{-1}$) at shorter wavelengths. This observation suggests that river profile geometries are scale-dependent and using small-scale observations to develop a general understanding of large-scale landscape evolution is not straightforward. At wavelengths >100 km, river profile geometries appear to be controlled by smoothly varying patterns of regional uplift and slope-dependent incision. Landscape simulations, based upon stream power that are externally forced by regional uplift do not exhibit a spectral transition from red to pink noise because these simulations do not incorporate heterogeneous erodibility. Spectral analysis of erodibility extracted from patterns of lithologic variation along river profiles suggests that the missing spectral transition is accounted for by heterogeneous substrates, which are characterized by white or blue noise ($\phi \propto k^0$ or k^1). Our results have implications for the way by which rivers record large-scale tectonic forcing while incising through complex lithologic patterns.

1. Introduction

A fundamental geomorphic concern is development of a quantitative understanding of the way in which tectonic and erosional processes combine to sculpt landscapes. Topographic evolution is of general interest since it plays a role in moderating environmental change as well as the distribution of natural resources and hazards. Longitudinal river profiles are particularly susceptible to environmental perturbations and are often exploited to investigate spatial and temporal patterns of regional uplift, biology, climate, hydrology, and substrate (e.g., Anderson & Anderson, 2010; Attal et al., 2008; Howard et al., 1994; Roberts et al., 2012; Whipple & Tucker, 1999; Whittaker et al., 2007, 2008; Zondervan et al., 2020). There is no accepted framework for understanding scales at which geologic and geomorphic processes combine to generate observed river profiles. For example, we currently do not understand, if it is reasonable to expect processes that operate at short (<10 km) spatial scales (e.g., plucking, abrasion, log jamming, block toppling, changes in substrate, waterfall formation) to scale or combine so that they generate observed shapes of river profiles at larger scales. In other words, it is not clear that erosional processes acting at small scales or variations in channel substrate combine to generate observed river profile shapes. Thus, the roles that different processes play in generating topography and landscape evolution remain hotly contested.

The focus of this contribution is to attempt to quantify scales at which river profiles are generated. This information will provide the means to define scales at which different processes (e.g., uplift, changes in substrate, or lithology) contribute to longitudinal river profiles. Scaling regimes are defined using river profiles from both large (>1,000-km long) and small North American rivers that traverse a variety of tectonic, geologic, and climatic realms (e.g., Columbia, Colorado, Mississippi, Nelson, Appalachian catchments). This approach does not require assumptions to be made about how landscapes evolve before exploring scaling regimes. An objective is to define universal behaviors of drainage patterns using the mapped spectral content of river profiles. Finally, we explore how a scale-dependent perspective of landscape evolution can be exploited to ensure that landscape simulations are consistent with observed landscapes over a significant range of scales (e.g., kilometers to thousands of kilometers).

© 2021. The Authors.

This is an open access article under the terms of the [Creative Commons Attribution License](https://creativecommons.org/licenses/by/4.0/), which permits use, distribution and reproduction in any medium, provided the original work is properly cited.

2. Background

2.1. Significance of Regional Uplift

From a geologic perspective, it is evident that regional uplift plays a central role in generating topography (e.g., England & Molnar, 1990; Holmes, 1945; King, 1978). Plate convergence, extension, and lithospheric strength are significant moderating influences (e.g., Cloetingh et al., 2005; Houseman & England, 1993; McKenzie, 1978). Subplate support by mantle convection can also generate topography with elevations of $O(1)$ km (order of magnitude 1 km) at margins and interiors of plates on length scales of up to $O(10^4)$ km (e.g., Burke & Gunnell, 2008; Hoggard et al., 2017; Japsen & Chalmers, 2000). Observational evidence and modeling results suggest that uplift rate histories play a key role in determining shapes of river profiles (e.g., Anderson & Anderson, 2010; Whittaker & Boulton, 2012). Generally accepted models of how river channels erode following uplift, or changes in base level, include transport-limited “diffusion” and detachment-limited (e.g., stream power) advective models (e.g., Whipple & Tucker, 1999, 2002). A three-dimensional formulation of landscape evolution (i.e., $z(x, y, t)$) that incorporates uplift and these generally accepted erosional models can be written as

$$\frac{\partial z}{\partial t} = -v(x, t) \left[A(x, t) P(x, t) \right]^m \nabla z^n + \kappa \nabla^2 z + U(x, t), \quad (1)$$

where z is elevation, t is time, v , m , n , and κ are erosional parameters that are calibrated using independent observations. A is upstream drainage area and P is precipitation rate, U is uplift rate, which varies as a function of space, x (upstream flow distance), and time (e.g., Braun & Sambridge, 1997; Hobbey et al., 2017; Salles, 2016; Tucker & Bras, 1998). ∇ and ∇^2 are maximum cell-to-cell slope and curvature. The first term on the right-hand side of Equation 1 is referred to as stream power erosion which predicts the headward advection of channel slopes (see e.g., Whipple & Tucker, 1999). The second term is erosional “diffusivity,” and is used to predict transport-limited erosion of hillslopes (Rosenbloom & Anderson, 1994). Values of erosional parameters, their spatiotemporal variability (or consistency), and their relationships to physical processes are debated (e.g., Anderson & Anderson, 2010; Attal et al., 2008; Howard et al., 1994). Optimal values appear to depend upon the scales at which observations are made or at which erosional models are calibrated (cf. Lague, 2014; Paul et al., 2014).

Equation 1 is often solved by assuming that river profiles are at steady state (i.e., $\partial z / \partial t = 0$), that $\kappa = 0$, and that the advective erosional parameters, uplift rate, and precipitation rate are either constant or take a simple form. An important advantage of exploiting inverse methodologies based upon integration to solve Equation 1 is that the assumption of steady state is not required and river channel heights are not differentiated in contrast with slope-area analysis (e.g., Schoenbohm et al., 2004). Results from both nonlinear and linear inverse modeling of drainage across a range of scales, for either individual river profiles or for continent-wide drainage inventories of thousands of profiles, highlight the importance of regional uplift in generating river profile shapes (e.g., Goren et al., 2014; Roberts & White, 2010; Roberts et al., 2012). These models are designed to seek the smoothest uplift rate history that yields the smallest residual misfit to families of observed river profiles (see e.g., Rudge et al., 2015). Results from those models suggest that long wavelength (>100 km) uplift can generate river profiles in multiple drainage basins that contain common shapes (e.g., Glotzbach, 2015; Goren et al., 2014; Pritchard et al., 2009; Roberts et al., 2012; Rudge et al., 2015). A benefit of using these models is that they generate a suite of predictions (e.g., uplift rate histories, incision rates, denudation, sedimentary flux) that can be tested with independent observations. For example, predicted uplift histories of North America are consistent with measurements from emergent Cretaceous to recent marine rocks (Fernandes et al., 2019).

From a geomorphic perspective, it is surprising that inverse models can be parameterized using a simple stream power formulation, and yet make meaningful predictions about uplift rate histories. Those results imply that recourse to spatially or temporally varying erosional processes, such as changes in bedrock strength, may not necessarily be required to match the shapes of river profiles at scales $\gtrsim 10$ km (see e.g., Fernandes et al., 2019; Roberts et al., 2012). Nonlinear inverse modeling has shown that models of fluvial erosion can successfully fit profile shapes without erosional “diffusivity” (i.e., $\kappa = 0$), recourse to shock wave behavior ($n \neq 1$, steeper slopes migrating faster than shallower slopes) or variable parameter values (v

is constant; e.g., Roberts et al., 2012; Rudge et al., 2015). Inverse modeling has also shown that meaningful (i.e., independently verifiable) histories of uplift can be obtained without requiring precipitation rate or drainage planforms to vary (e.g., Fernandes et al., 2019; Rudge et al., 2015). More formally, these studies indicate that a one-dimensional formulation contains enough complexity to match most observed river profiles such that

$$\frac{\partial z}{\partial t} = -vA^m \frac{\partial z}{\partial x} + U(x,t), \quad (2)$$

where $m \sim 0.25-0.5$, $A = A(x)$, and x is distance along a river. These models satisfactorily match the “overall” (i.e., long wavelength, >100 km) river profile shapes but are poorer at capturing rapid changes in relief. A corollary is that Equation 2 is a good representation of how landscapes evolve at large scales even though it inevitably oversimplifies river profile evolution at smaller scales. It does not explicitly contain the multitude of physical, chemical, and biotic processes that determine evolution at such scales (e.g., Lamb & Dietrich, 2009; Lamb et al., 2008; Turowski et al., 2007).

2.2. Erosional Processes and Heterogeneous Substrates

Hydraulic, biotic, geomorphic, and climatic processes influence landscape development on a range of scales (e.g., Anderson & Anderson, 2010; Attal et al., 2008; Braun, 2002; Whipple & Tucker, 1999; Whittaker & Boulton, 2012; Willett et al., 2014). Numerous studies emphasize the importance of erosional processes and changes in erodibility of the substrate which to some extent, tends to downplay or even neglect the influence of regional tectonic uplift (e.g., Baldwin et al., 2003; Gallen, 2018). Erosional complexity, stochasticity, and threshold behavior are thought to be dominant over a range of scales, and as a consequence, inverse modeling schemes that exploit simple erosional models are not universally accepted.

Processes driving fluvial erosion are often investigated by transforming topography using modeled landscape metric measures (e.g., k_{sn}, χ). Variability is examined by making the stream power model more complex by including, e.g., slope-dependent velocity ($n \neq 1$), erosion thresholds, and spatiotemporally varying erosional parameter values. Sometimes, model predictions are tested against independent observations, in order to objectively test assumptions. Driving processes can be investigated by correlating river shapes with independent observations. For example, correlation of bedrock strength measurements along the Colorado River has been interpreted, as an indication that lithology is the dominant control of river profile geometry (Bursztyn et al., 2015). Similarly, correlations between longitudinal profiles and substrate of Appalachian rivers have been interpreted as an indication of the general importance of bedrock in controlling river profile shapes (Gallen, 2018). DiBiase et al. (2018) used in situ ^{10}Be concentrations in stream sands from nested watersheds of the Young Womans Creek, which is a tributary of the West Branch Susquehanna River that drains the unglaciated Appalachian Plateau, to argue that lithologic boundaries between Paleozoic strata control the location of changes in erosion rate, and fluvial and hillslope morphology. Zondervan et al. (2020) used measurements of substrate strength and hydraulic geometries in the Vouraikos catchment, which drains into the Gulf of Corinth, Greece, to calibrate a stream power model and compare the position of observed and predicted knickpoints. They suggest that lithology plays a fundamental role in determining the pace of fluvial erosion. Changes in the substrate have also been related to changes in channel widths. For example, Spotila et al. (2015) argue for lithologic control of river morphology based on correlation of channel aspect ratio (width/depth) and bedrock lithology, and that changes in channel width do not necessarily reflect variations in uplift rate, but instead may result from a complex response to bedrock properties.

An apparently straightforward relationship between substrate and topographic relief seems obvious, uncontroversial, and forms the basis for many geomorphic studies (e.g., Campforts et al., 2020; Sklar & Dietrich, 2001; Yanites et al., 2017). However, the meaning of such correlations is not straightforward since similar river profiles can be due to different processes (e.g., Whipple & Tucker, 1999). For example, the shape of the Colorado River and the Grand Canyon knickzone could be caused by regional uplift (see e.g., Crow et al., 2014; Roberts et al., 2012). Moreover, changes in substrate do not correlate with changes in relief or erosional processes in many places. For example, Gallen et al. (2011) examined the relationship between topographic metrics, knickpoint location, and landslide distribution for the Cullasaja basin in the upper

reaches of the Little Tennessee River and suggested that local base-level fall, rather than bedrock lithology, controls development, and propagation of knickpoints. Duxbury et al. (2015) performed cosmogenic ^{10}Be analysis of bedrock and sediment from rivers of the Central Appalachian Mountains which showed that there is no obvious difference in erosion rates measured in catchments where different lithologies are incised (e.g., granite, metabasalt, quartzite, siliciclastic rocks).

Despite these studies, it is not clear, how estimates of rock strength can be related to erodibility on the spatial and temporal scales at which drainage evolves. It is unclear how spot measurements of rock or joint strength can be related to erosion rate, $E(x, t) = \partial z / \partial t$. A central problem is that we do not know, if erosion or strength measurements from spot locations scale such that they can be used to reliably predict river profiles. For example, laboratory experiments in which saltating grains impact bedrock show that erosion rate is negatively correlated with tensile strength (e.g., Sklar & Dietrich, 2001). However, at larger scales rivers flowing over ostensibly strong rock (e.g., fresh basalt) can rapidly (essentially instantaneously) erode $O(1-10)$ m as competent columns topple (e.g., Stucky de Quay et al., 2019). This topic has been investigated to some extent by changing parameters in advective stream power erosional models (e.g., Yanites et al., 2017). Increasing or decreasing the values of parameters that control rates at which slopes propagate upstream (e.g., prefactor v in Equation 2) affects theoretical river profile shapes. However, it is not clear from such theoretical approaches that measurements of rock strength can be converted into values of v (or erodibility) from first principles. Unfortunately, it is not obvious what independent data can be brought to bear to assess the values of erodibility used in such studies, and this problem is especially difficult to address on the length and time scales at which large rivers erode, e.g., $O(10^2-10^3)$ km, $O(1-100)$ Ma. It is also unclear at what scales precise values of these parameters or their integrated (i.e., average) quantities matter for how river profiles acquire their shapes (e.g., Paul et al., 2014). Clearly, developing a framework to understand how river profile shapes are generated across the scales of interest is an important problem. One way to address this challenge is to quantify the scales at which river profiles are generated. Such a framework could then be used to examine correlative, independent, observations of, for example, uplift and lithology at appropriate scales.

2.3. Spectral Analysis

Topographic scaling can be investigated by transforming one-dimensional or two-dimensional data sets into the spectral domain, namely, $z(x)$ is transformed into $z(k)$ or $z(x, k)$, where z is elevation, x is distance, and k is wave number (spatial frequency; e.g., Bell, 1975; Birnir et al., 2001; Pelletier, 1999; Perron et al., 2008; Singh et al., 2011). Previous geomorphic studies using wavelet transforms have shown that, for large African rivers, most spectral power occurs at wavelengths $\gtrsim 100$ km (Roberts, 2019; Roberts et al., 2019). At these scales, river profiles are characterized by red noise where spectral power (height-squared), $\phi \propto k^{-2}$. At shorter length scales (higher wave numbers), there is a transition to pink noise where $\phi \propto k^{-1}$, which can be generated by combining red with white noise (ϕ independent of k) and/or blue noise ($\phi \propto k$). A spectral slope of -2 means that the amplitude of topographic features is proportional to their horizontal length. In contrast, a spectral slope of 0 (i.e., white noise) is generated by features with amplitudes that are independent of their horizontal length. Spectral slopes of 1 (i.e., blue noise) implies that amplitudes increase as wavelengths get shorter, which is characteristic of shock wave behavior. These results suggest that regional uplift, which has an approximately red spectrum, dominates at long wavelengths. Substrate variability and erosional processes, which may have a white/blue spectrum, become emergent at shorter wavelengths (Roberts et al., 2019). Numerical models that incorporate stream power erosion and quenched noise can generate realistic river profiles (Lipp & Roberts, 2021; Roberts et al., 2019).

The purpose of this manuscript is to build upon these spectral approaches. One objective is to quantify the length scales, locations, and amplitudes at which contributors, such as regional uplift and lithology, shape the longitudinal profiles of North American rivers. Wavelet transforms are developed and applied to rivers including the Arkansas, Columbia, Colorado, Cumberland, Mississippi, Missouri, Nelson, North and South Platte, Allegheny, and Kanawha branches of the Ohio, Rio Grande, and Tennessee (Figure 1). Rivers draining the Appalachian Highlands (Ocmulgee, Savannah, Santee, Roanoke, James, Potomac) are transformed and their cross-wavelet power spectra are used to quantify similarities and dissimilarities of river profiles from an orogenic belt. Results are used to examine the origins of similar geometries of familial river profiles. We then explore how observed spectra can be generated using landscape evolution models that incorporate

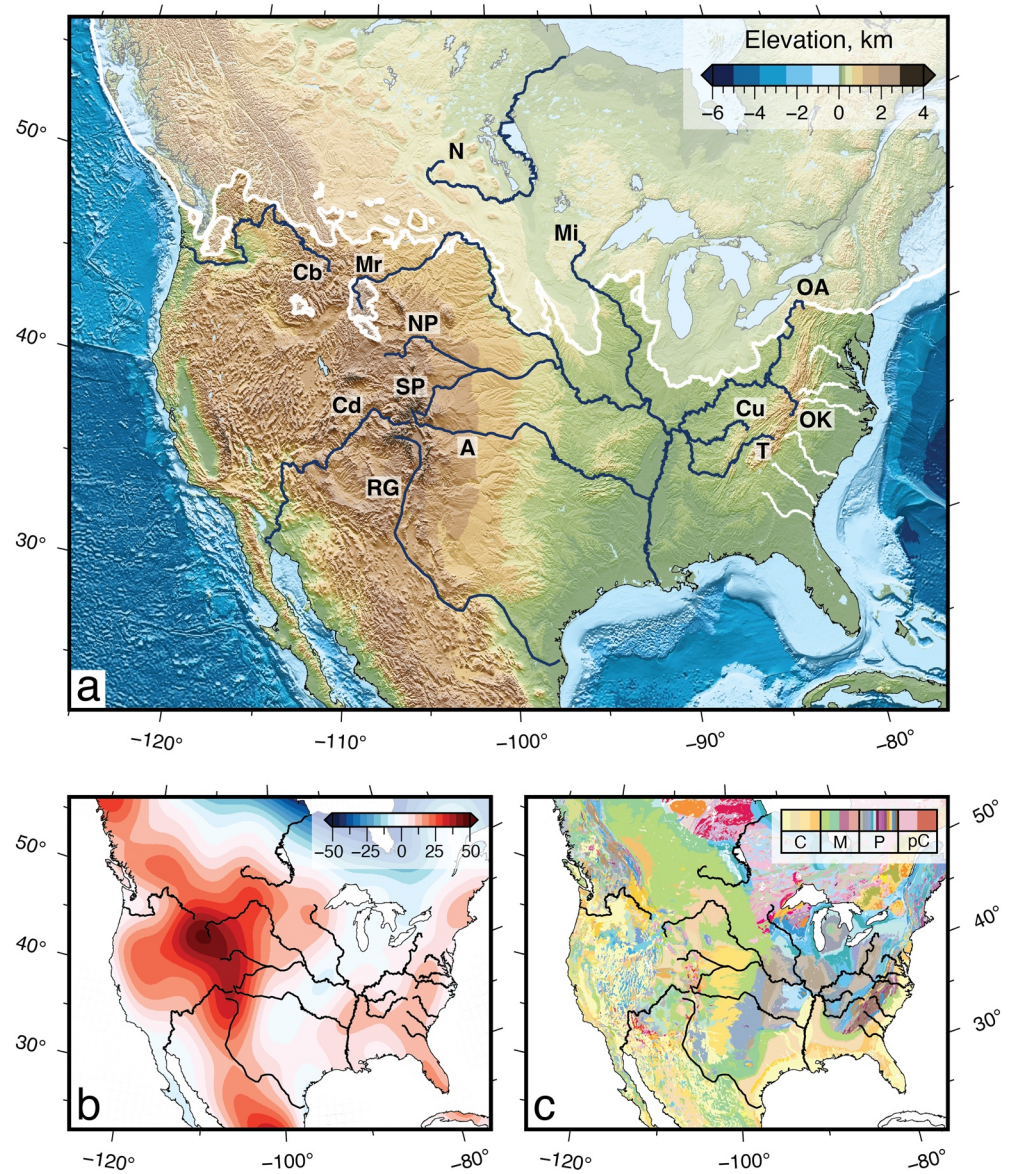


Figure 1. North American Drainage. (a) Topographic map from ETOPO1 database of North America showing selected rivers (blue lines). A = Arkansas, Cb = Columbia, Cd = Colorado, Cu = Cumberland, Mi = Mississippi, Mr = Missouri, N = Nelson, NP = North Platte, OA/OK = Allegheny/Kanawha tributaries of Ohio, RG = Rio Grande, SP = South Platte, T = Tennessee, white lines = Appalachian rivers (Figure 7), translucent polygon = extent of Laurentide Ice Sheet during Last Glacial Maximum (Batchelor et al., 2019). (b) Long-wavelength free-air gravity from gravity recovery and climate experiment (GRACE) database (Tapley et al., 2005); units of scale bar in mGal. (c) Geologic map of North America (ngmdb.usgs.gov/gmna; Garrity & Soller, 2009). C/M/P/pC = Cenozoic/Mesozoic/Paleozoic/Precambrian.

uplift and changes in substrate erodibility. Scales at which changes in erodibility contribute to topographic relief are quantified and amplitudes at which these changes are manifest in river profiles are estimated. Finally, a probabilistic view of landscape evolution is developed, which incorporates appropriately scaled processes from short (<10 km) to long (>1,000 km) wavelengths. We conclude by discussing how this approach helps to bridge scale-dependent insights into how fluvial topography is generated.

3. Observations and Methodology

3.1. Digital Elevation Model

River profiles were extracted from the ASTER (Advanced Space-borne Thermal Emission and Reflection Radiometer) global digital elevation model, which has a vertical accuracy and horizontal resolution of $\sim\pm 8$ and 75 m, respectively (Tachikawa et al., 2011). Flow directions were calculated using the D8 algorithm from the ArcGIS libraries (Tarboton, 1997).

Figure 1a presents North American topography together with the major rivers that were transformed in this study: Arkansas, Columbia, Colorado, Cumberland, Mississippi, Missouri, Nelson, North and South Platte, Allegheny, and Kanawha branches of the Ohio, Rio Grande, Tennessee. These rivers traverse a variety of physiographic and geologic environments, some of which were affected ~ 20 ka ago at the Last Glacial Maximum of the Laurentide Ice Sheet (Figure 1a, Gao, 2011; Wickert, 2016). They also drain regions of probable dynamic and tectonic support (Figure 1b). Figure 1c shows the location of these rivers superimposed upon a geologic map of North America (GMNA; Garrity & Soller, 2009). The six Appalachian rivers analyzed here flow from the Appalachian Mountains before traversing the Atlantic Coastal Plains and draining into the Atlantic Ocean; names and classification of physiographic provinces follow Fenneman (1928).

3.2. Channels in Frequency Domain

To determine scales at which river profiles are generated, their longitudinal profiles are transformed from the spatial domain, $z(x)$, into the space-wave number domain, $Z(k)$. Perhaps more conceptually simple is to first consider converting rivers into the wave number (i.e., spatial frequency) domain using, for example, a Fourier transform (e.g., Roberts, 2019). Transformation of rivers into the Fourier wave number domain, $Z(k)$, should result in no change in total spectral power, P_T , since

$$P_T = \int_{-\infty}^{\infty} |z(x)|^2 dx = \int_{-\infty}^{\infty} |Z(k)|^2 df. \quad (3)$$

Power at a given wave number interval, P_z , is given by

$$P_z(f) = 2 |Z(k)|^2, \quad 0 \leq k \leq \infty. \quad (4)$$

Interpreting power spectra using typical Fourier techniques is challenging for theoretical and practical reasons. First, river profiles are evidently not analogous to stationary functions: they do not, for example, start and end at the same elevation. Second, a well-known issue with power spectra generated by Fourier transform is power leakage from one wave number to another. Finally, calculated power spectra can be noisy. These problems make it challenging to identify sources of power and spectral regimes from transformed profiles based on periodic trigonometric basis functions. An alternative approach is to exploit wavelet transforms.

The continuous wavelet transform, $W_x(s)$, provides a means to determine spectral power as a function of wavelength and distance along river channels (e.g., Daubechies, 1990). Heights are first linearly resampled at a fixed horizontal resolution δx , and then mirrored, before being transformed. In this study, the data were linearly resampled such that $\delta x = 2$ km. The transformation yields estimates of power (ϕ) at evenly spaced positions, as a function of scale s . The transformation in discrete form is given by

$$W_x(s) = \sum_{x'=0}^{N-1} z_{x'} \psi \left[\frac{(x' - x)\delta x}{s} \right], \quad (5)$$

where N is the number of data points, $z_{x'}$ are discrete measurements of elevation along the profile, ψ is a wave function, which is scaled by s and translated along the profile by x' . We systematically tested a range of “mother wavelets” (i.e., basis functions) by changing dimensionless frequencies $\omega_0 = 4, 6, 8$ and orders $M = 2, 4, 6, 8$ of the Morlet and DOG (derivative-of-Gaussian) wavelets, respectively. Wavelet resolution was set to $\delta_j = 0.1$ (Torrence & Compo, 1998). The wavelet power spectrum is given by $\phi(s, x') = |W_x(s)|^2$.

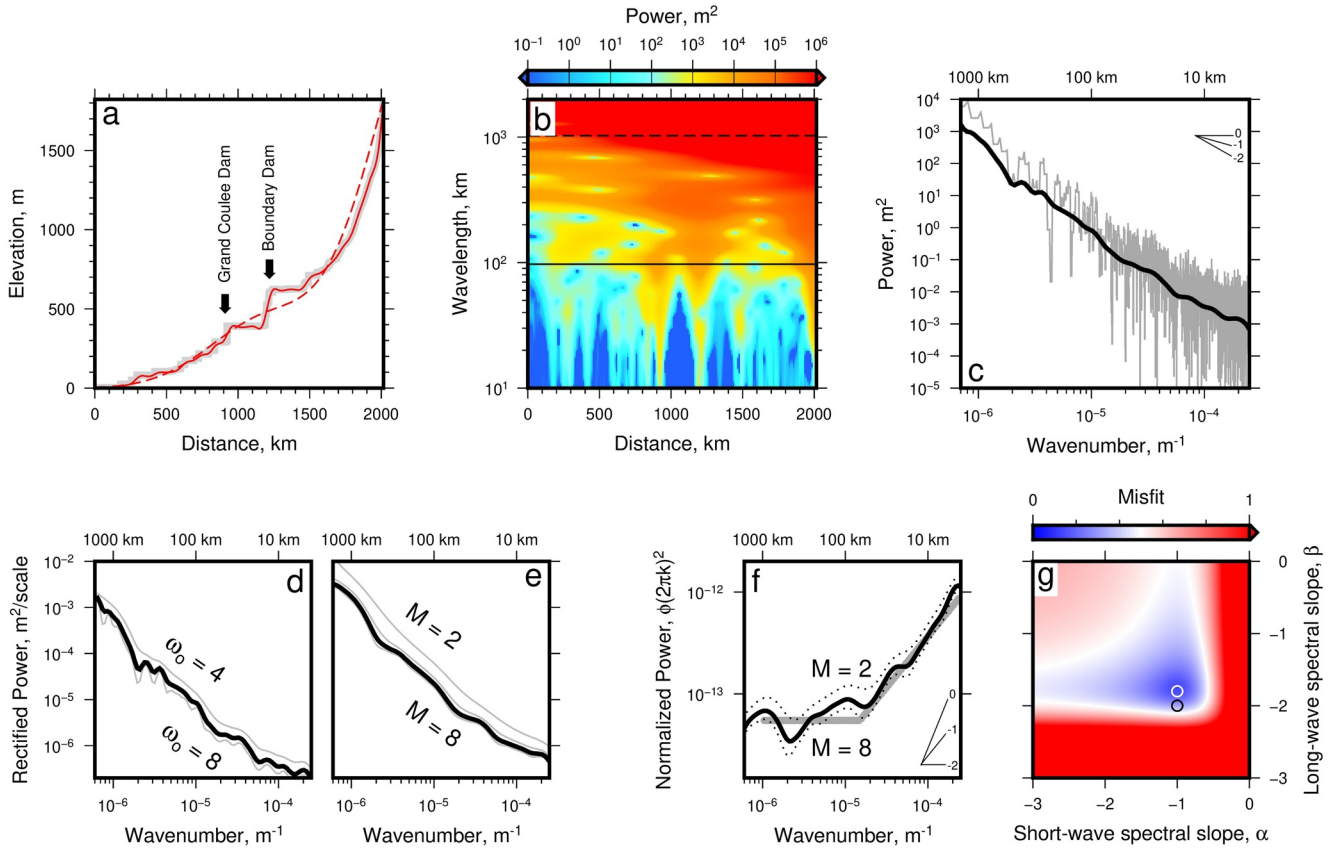


Figure 2. Wavelet transforms of Columbia River. (a) Gray line = longitudinal river profile extracted from Advanced Space-borne Thermal Emission and Reflection Radiometer (ASTER) Global Digital Elevation Model (GDEM) database (Tachikawa et al., 2011). Labeled black arrows indicate man-made dams; red solid and dashed curves = inverse wavelet transform for wavelengths >100 and $>1,000$ km, respectively. (b) Power spectrum calculated using Morlet wavelet; dimensionless frequency, $\omega_s = 6$. Solid and dashed lines = lower bounds on filters used to generate river profiles in panel (a). (c) Black line = distance-averaged wavelet power spectrum as function of wave number, (k) gray line = five point moving average of power spectrum generated from Fourier transformation of river profile. Spectral slopes, where power, $\phi \propto k^\beta$ for red ($\beta = -2$), pink ($\beta = -1$), and white ($\beta = 0$) noise are shown. (d) Rectified power as function of wave number, $\phi_r(k)$; $\omega_s = 6$ (black) or $\omega_s = 4, 8$ (gray) (Liu et al., 2007). (e) Rectified power, ϕ_r , calculated using M th order derivative-of-Gaussian (DOG) wavelets; $M = 6$ (black) or $M = 2, 4, 8$ (gray). (f) Identical spectra normalized by $(2\pi k)^2$ (i.e., flattened on red noise; black curve: $M = 6$; dotted curves: $M = 2, 8$); note inset spectral slopes. Gray line = best-fitting two-component model with integer spectral slopes indicated by black circle in panel (g). (g) Misfit between observed and calculated power spectra using two-component model. α and $\beta =$ two different spectral slopes; white circle = best-fitting model; black circle = best-fitting model for integer slopes.

Distance-averaged power spectra generated from transformed spatial series, $\bar{\phi}(s)$, which are conceptually similar to results of the Fourier transform, can be calculated using

$$\bar{\phi}(s) = \frac{1}{N} \sum_{x=0}^{N-1} |W_x(s)|^2. \quad (6)$$

Resulting power spectra can be compared to Fourier power spectra by converting scales, s , into wave numbers and rectifying spectral bias (e.g., Liu et al., 2007; Torrence & Compo, 1998). Scales were calculated following Torrence and Compo (1998) where $s_j = s_0 2^{j\delta_j}$ where $j = 0, 1, \dots, J$. The smallest scale $s_0 = 2\delta x = 4$ km, and maximum scale J is determined by the number of elevation measurements. A known bias introduced by wavelet transformation is that calculated power can be dependent upon the scale being examined. This bias is trivial to rectify by dividing power, $\phi(x, k)$, by the scale with which it is associated. Rectified power is calculated so that $\phi_r = \bar{\phi}(s) |Ns|^{-1}$.

Examples of applying these spectral methods to the Columbia River are shown in Figure 2. Figure 2a shows the profile of the Columbia River extracted from the ASTER Global Digital Elevation Model (GDEM) (see Figure 1a). The inverse transform is performed by summing the wavelet transform, W_x , for all scales, s , at

each distance, x , along the profile (Equation 6). The inverse transform calculated using all scales from s_0 to J faithfully matches the original profile (Section 3.3). Figure 2a also shows the inverse wavelet transform calculated using only wavelengths >100 and $>1,000$ km, respectively. Figure 2b shows the wavelet power spectra of the Columbia River generated using a Morlet wavelet with $\omega_0 = 6$. The solid and dashed lines show the lower limit of the filters used to generate the corresponding profiles shown in panel a. The black curve in panel (c) shows the distance-averaged power spectrum generated from the wavelet transform shown in panel (b). White, pink, and red noise spectral slopes are indicated by the legend labeled 0, -1 , and -2 in the top right of panel (c). Figure 2c shows an example of a Fourier transform of the mirrored Columbia River profile. Figures 2d and 2e show distance-averaged power spectra generated using wavelets with different dimensionless frequencies and orders (see labels and caption to Figure 2). These panels show rectified power spectra. Note that the power spectra converge with dimensionless frequencies and orders ≥ 6 .

Figure 2f shows the rectified DOG spectrum normalized by $(2\pi k)^2$ such that red noise, $\phi \propto k^{-2}$, is a horizontal line. The gray dog-leg line shows the best-fitting two-component spectral model with integer slopes. This model was generated by sweeping the parameter space shown by the axes of Figure 2f for best-fitting hinge position, and allowing spectral slopes of the two components, α and β , to vary independently (see Roberts et al., 2019). The spectral slopes α and β are the short-wavelength and long-wavelength components, respectively. The best-fitting integer slopes are shown by the black circle. The best-fitting noninteger spectral slopes are indicated by the white circle in panel (g). The color scale in this figures shows misfit between observed (black curve in panel f) and theoretical (gray line) spectral slopes for the best-fitting hinge position, where the two theoretical spectral slopes meet in panel (f). Figure 3 shows examples of river profiles, inverse wavelet transforms, wavelet transforms, flattened rectified spectra, and best-fitting theoretical spectra for the other 12 large rivers of this study, including the Colorado, Mississippi, and Nelson rivers (Figure 1a).

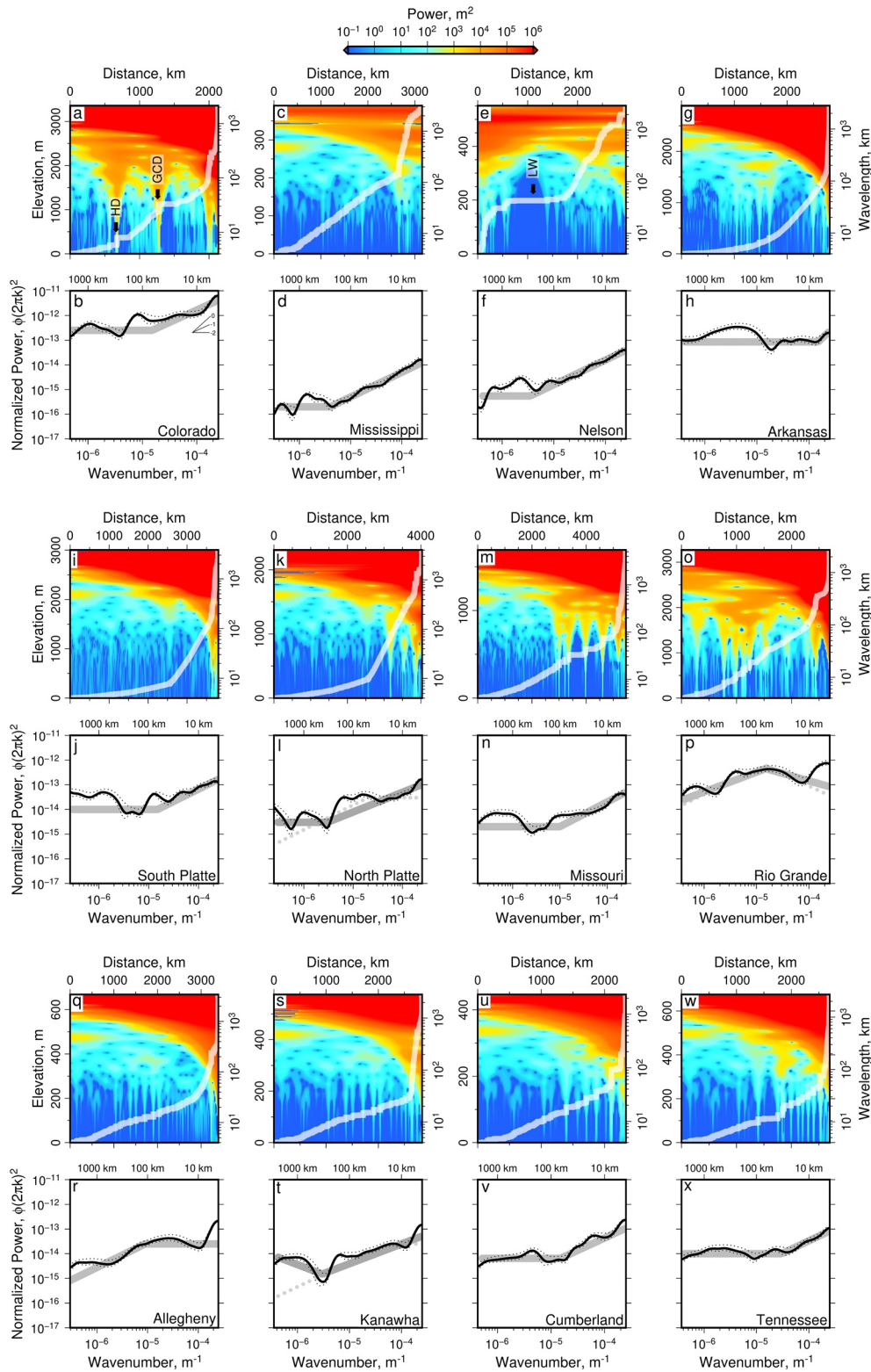
3.3. Uncertainties

There are three important sources of uncertainty. First, the vertical error of ASTER GDEM data, Δz , is $\sim \pm 8$ m, which suggests that the uncertainty in calculated power ϕ is ~ 64 m² (Tachikawa et al., 2011). Roberts et al. (2019) suggested that one way to assess the impact of this source of error was to remove parts of the transformed power spectra with power less than, say, 100 m², and insert random noise with distributions equivalent to those in the digital elevation data. They found that adding or removing noise in this way did not materially affect conclusions drawn from fitting observed spectra.

Second, satellite measurements can underestimate changes in elevation over minor distances, e.g., the depths of narrow gorges. Furthermore, ASTER GDEM data record heights to the top of the water column, and this method assumes these heights equate to bathymetry. The difference in height from the bottom to the top of the water column tends to be small enough that it does not affect calculated spectra at the scales we consider (Roberts et al., 2019). We have tried to avoid large deep lacustrine settings. The biggest water body encountered is Lake Winnipeg, which has an average depth of 9–14 m, which is unlikely to affect our principal conclusions but will mean that short-wavelength power is underestimated in its vicinity (see Figure 3e). Similarly, short-wavelength power beneath other lakes is underestimated, but unlikely to affect our principal conclusions since these bodies occupy relatively short portions of the river profiles.

Third, applying spectral techniques to signals with large amplitudes close to the start or end of spatial series (e.g., headwaters of longitudinal river profiles) generates edge effects (e.g., artificially high power in some parts of calculated spectra). Potentially problematical regions can be mapped using cones of influence (see e.g., Torrence & Compo, 1998). Mirroring is an alternative means to mitigate edge effects (Roberts et al., 2019). Spectral leakage is also reduced by mirroring and choosing appropriate basis (e.g., mother wavelet) functions.

The significance of these sources of error can be assessed by performing inverse wavelet transforms. Inverse transformation of the power spectra of North American rivers recovers original signals (longitudinal profiles) to a mean error of 0.3% when ω_0 and $M = 6$. Thus, calculated power spectra are high fidelity forms of observed river profiles. The inverse transform of all spectra summed over all k for wavelengths ≥ 100 and $\geq 1,000$ km is shown with the actual profile in Figure 2a. For the Columbia River, the filtered inverse wavelet transforms closely match the long-wavelength shapes of observed longitudinal profiles (Figure 3).



3.4. Uplift and Erodibility

To investigate the source of power along North American river profiles, we examined two potential candidates: uplift and bedrock erodibility. First, we examine the spectral content of synthetic river profiles generated from an uplift rate history that best fits a continent-wide inventory of 4,161 river profiles (see Figure 4). The model and its calculated uplift history are described in detail by Fernandes et al. (2019). Figures 4a–4f show a subset of the observations and best-fitting river profiles used to generate the calculated uplift history. The model was parameterized using a calibrated version of Equation 2 and solved using a damped linearized inverse model (Figure 4, Fernandes et al., 2019; Rudge et al., 2015). The predicted uplift history has been tested using independent stratigraphic information from a continent-wide inventory of paleobiological observations (Figures 4g–4l, see Fernandes et al., 2019). The spectra, ϕ_f , for the optimal “Columbia” profile are shown in Figures 5a–5c. Spectra for the “Colorado,” “Mississippi,” and “Nelson” rivers are in the Supporting Information. Spectra show that the greatest power occurs at wavelengths >100 km and that these spectra are characterized by red noise. When compared to the power spectrum of the Columbia River, the same high power occurs at longer wavelengths but spectral power at wavelengths $<O(10^2)$ km is diminished (Figure 2).

Second, jointing and fracturing of rock, heterogeneities, and changes in exposed bedrock with time make it challenging to confidently estimate substrate erodibility along a given river profile. One approach is to explore empirical schemes that relate rock strength to lithology (e.g., Moosdorf et al., 2018; Sklar & Dietrich, 2001). To do so, we convert a geologic map into a map of erodibility using the approach described by Campforts et al. (2020) (Supporting Information). We favor this approach since they explicitly convert geologic outcrop into erodibility. This methodology assumes that rock strength, and by inference erodibility, is a function of lithology. Igneous rocks are classed as strongest with an effective strength unaffected by age. Rock strength decreases for metamorphic, sedimentary rocks, and unconsolidated sediments. In this scheme, increasing the age of nonigneous rocks increases strength in an approximately exponential way. This scheme is broadly consistent with interpretation of rock strength measurements from the Colorado Plateau. For example, Bursztyn et al. (2015) suggested that tensile rock strength data showed that older, deeply buried rocks are generally stronger than younger rocks, with the exception of limestone and Quaternary basalt. We acknowledge that alternative schemes exist that incorporate weathering of basaltic rock, jointing, and dipping strata. Description of geologic age, lithology, and assigned erodibility value for each rock unit is provided in the Supporting Information. The resulting lithologic erodibility values are 0.286–1.714. These dimensionless values can be incorporated into landscape evolution models (see Campforts et al., 2020). The smallest resolvable geologic feature on the geologic map is ~ 10 -km wide, which is appropriate for the sampling interval of the river profiles that we investigate. We note that there is a weak negative correlation between observations of rock strength measurements collected along the trunk of the Green-Colorado River, and erodibility calculated from the geologic map (Supporting Information; $R^2 = 0.2$ for tensile and compressive strength, respectively, cf. Bursztyn et al., 2015; Campforts et al., 2020).

A reasonable assumption is that changes of slope are generated where erodibility changes, ΔE . Thus we investigate the spectral content of the $\Delta E = E_i - E_{i-1}$ spatial series (see Figure 5d). Figures 5d–5f show the results from transforming changes in erodibility along the Columbia River. Figure 5d shows substrate colored by age along the river profile (see Figure 1). The power spectrum of changes in lithological erodibility along the river profiles examined here have greatest power at wavelengths <100 km, and have blue or white spectral slopes. These results suggest that combining spectra of synthetic river profiles generated by smoothly varying uplift rate histories with erodibility spectra can reproduce the scaling of observed river profiles.

Power spectra of best-fitting profiles from Figure 5b can be combined with scaled versions of the power spectra of the erodibility spatial series (Figure 5e) by simple addition where $\phi_M(x, k) = \phi_f(x, k) + \phi_{\Delta E}(x, k)$

Figure 3. Wavelet transforms of North American river profiles. (a) Translucent white curve = profile of Colorado River extracted from Advanced Space-borne Thermal Emission and Reflection Radiometer (ASTER) Global Digital Elevation Model (GDEM) database. Arrows indicate man-made dams: HD = Hoover Dam, GCD = Glen Canyon Dam; color map = power spectrum calculated using Morlet wavelet ($\omega_s = 6$). (b) Distance-averaged spectra of Colorado River rectified and then normalized by $(2\pi k)^2$; black curve = $M = 6$, dotted curves = $M = 2$ and 8. Note that inset spectral slopes: 0/−1/−2 = white/pink/red noise. Gray line = best-fitting two-component model with integer spectral slopes. (c–x) River profiles, power spectra, and distance-averaged spectra for annotated North America river profiles (Figure 1). Gray lines = best-fitting two-component spectral models with integer slopes; LW = Lake Winnipeg. Panels (l), (p), and (t) solid gray lines = best-fitting two-component (noninteger) spectral models; dotted lines = best-fitting models with integer spectral slopes.

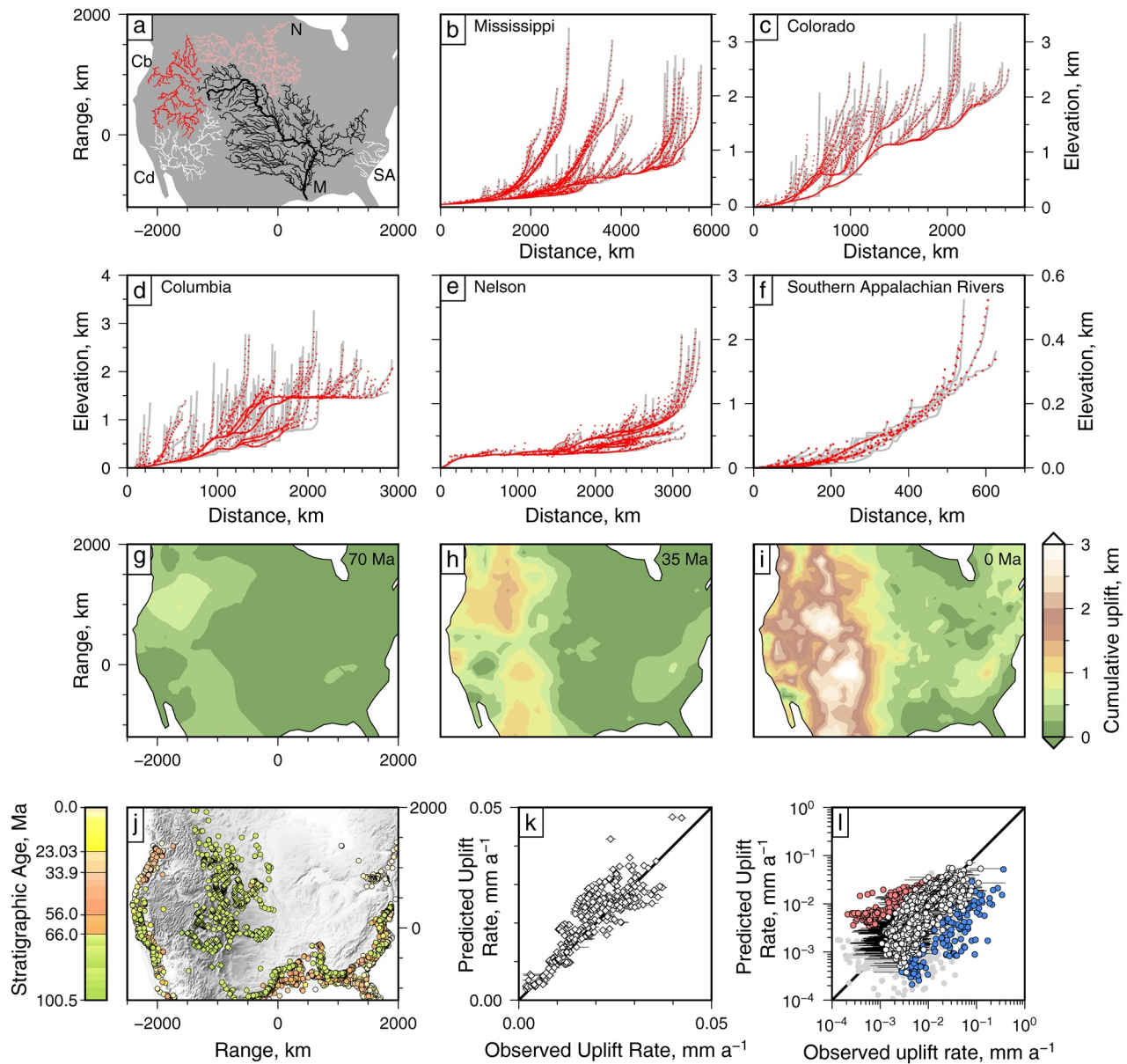


Figure 4. North American drainage patterns and uplift history. (a) Major catchments extracted from Advanced Space-borne Thermal Emission and Reflection Radiometer (ASTER) Global Digital Elevation Model (GDEM) database. Cb = Columbia, Cd = Colorado, M = Mississippi, N = Nelson, SA = Southern Appalachian. Albers equal area projection. (b) Observed (gray) and calculated (red dots) river profiles for Mississippi, (c) Colorado, (d) Columbia, (e) Nelson, and (f) southern Appalachian catchments. Best-fitting profiles generated by linear inverse modeling of 4,161 river profiles (see e.g., panels g–i; residual rms misfit = 1.25; Fernandes et al., 2019). (g–i) Calculated cumulative uplift history at 70, 35, and 0 Ma, respectively. (j) Colored circles and diamonds = marine fossil assemblages extracted from Paleobiology database and marine to nonmarine stratigraphic transitions, respectively (colors indicate depositional age). (k–l) Comparison of time-averaged uplift rate from inverse model and stratigraphic observations (diamonds in panels j and k) and biostratigraphic observations (circles in panels j and l). White circles in panel (l) = results that agree with stratigraphic estimates; red/blue circles = inverse model that over/underpredicts uplift rate by factor of >2; black lines = 1:1 relationship (Fernandes et al., 2019).

(Figure 5g). The distance-averaged power spectrum of this model is presented in Figure 5h, where it is compared with the power spectrum of the Columbia River. Figure 5i shows the difference between the power spectra for the actual Columbia River and for the model. Results for the Columbia, Mississippi, and Nelson River are presented in Supporting Information.

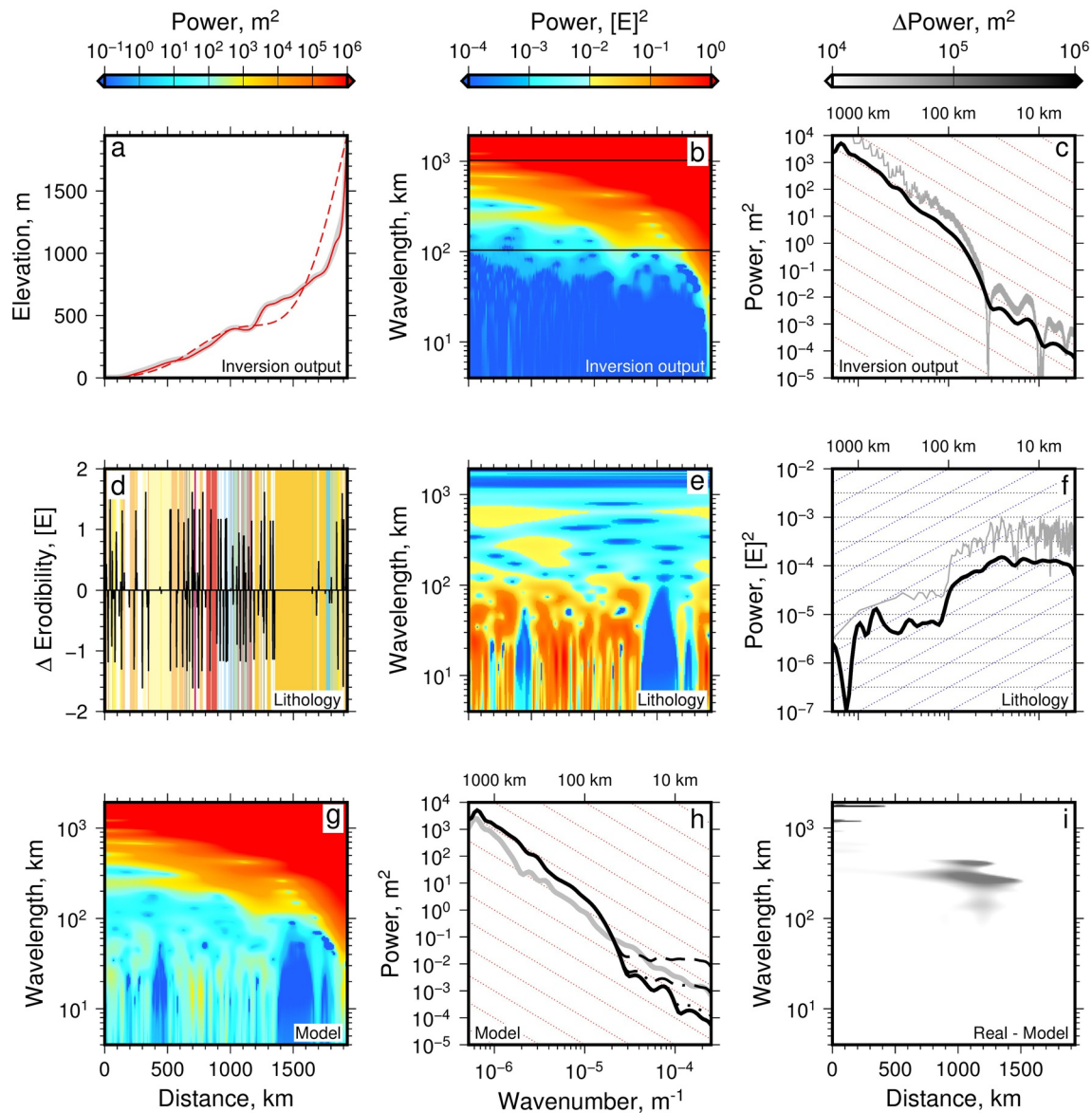


Figure 5. Wavelet transform of calculated profile and lithology along Columbia River. (a) Gray = best-fitting “Columbia” profile generated by uplift history shown in Figure 4. Red solid and dashed curves = inverse wavelet transform for wavelengths >100 and >1,000 km, respectively. (b) Power spectrum of profile calculated using Morlet wavelet ($\omega_s = 6$). Solid and dashed lines = lower bounds on filters used to generate river profiles in panel (a). Color scale is shown top left. (c) Black line = distance-averaged power spectrum of calculated river profile as function of wave number, k ; gray line = five point moving average from Fourier transformation (FFT). Dotted graticule = red noise power spectrum (i.e., power, $\phi \propto k^{-2}$). (d) Colored “bar-code” = lithology along the Columbia River extracted from geologic map of North America (GMNA) database (see Figure 1c for key and references). Black curve = erodibility differences: $\Delta E = E_i - E_{i-1}$ (see text). (e) Power spectrum of erodibility spatial series. Color scale = top middle. (f) Black line = distance-averaged power spectra of ΔE spatial series; gray line = FFT of erodibility spatial series. Dotted black/blue graticule = white/blue noise spectra (i.e., $\phi \propto k^0$, $\phi \propto (k)$). (g) Power spectra generated by combining spectra of calculated river profile and scaled version of lithologic spatial series (see text for details). (h) Gray line = distance-averaged power spectrum of Columbia River profile (see Figure 2). Black curve = power spectrum for calculated river profile (panel c). Dashed/dot-dash/dotted curves = power spectra for combined spatial series. (i) Difference between power spectra of observed and calculated river profiles, Δ Power; color scale = top right. Calculated differences between observed and calculated spectra are provided for Colorado, Mississippi, and Nelson rivers in Supporting Information.

3.5. Forward Models of Landscape Evolution

In order to investigate causes of observed spectral regimes, we exploit forward simulations of landscape evolution. Synthetic landscapes are generated using the Basin and Landscape Dynamics (Badlands) algorithm developed by Salles (2016). Although the Badlands algorithm includes a range of possible erosion models, we focus on the linear stream power formulation which assumes that $n = 1$ and that hillslope erosion can

be described using a diffusional creep process (Smith & Bretherton, 1972; Tucker & Bras, 1998; Whipple & Tucker, 1999). Change in the elevation of a given cell within Badlands is given by

$$\frac{\partial z}{\partial t} = -v(AP)^m \nabla z - \kappa \nabla^2 z + U(x, y, t) + \eta(x, y, t). \quad (7)$$

Most parameters are identical to those used in Equation 1. Slope, ∇ , and curvature, ∇^2 , are the maximum changes between a given individual cell and surrounding cells, according to the single-flow direction algorithm of Braun and Willett (2013). η is additive noise, which can be designed to generate river profiles that have the same spectral content as observed profiles. We can also test whether different distributions of erosional parameter values (e.g., v scaled by erodibility or by random noise) can generate observed power spectra since Badlands can include spatially variable v on a point-wise basis.

We start by setting uplift rate forcing, U , using results from inverse modeling of a continent-wide inventory of longitudinal river profiles for North America (Figure 4, Fernandes et al., 2019). This forcing is applied across a triangulated network generated from vertices with a regular spacing of 10×10 km (Salles, 2016). We use an output time interval of 5.9 Ma, but the chosen model time step length is subject to the Courant-Friedrichs-Lewy stability condition and is smaller than 5.9 Ma (Courant et al., 1967). We use a small value of $\kappa = 10^{-20} \text{ m}^2 \text{ yr}^{-1}$ to ensure stability and to approximate the parametrization of the inverse model (Fernandes et al., 2019; Rudge et al., 2015; Salles, 2016). Sea level is assumed to be invariant. Precipitation rate, $P = 1 \text{ m yr}^{-1}$, is constant. No adjustments are explicitly made to mimic reorganization of paleocoastlines, glacial erosion, or the flexural response to changing crustal loads as the landscape evolves (cf. Salles et al., 2017). Erosional parameter values of v , m , and n are constant: $0.99 \text{ m}^{0.2} \text{ Ma}^{-1}$, 0.4, and 1, respectively (Fernandes et al., 2019). Dynamic evolution of drainage, including drainage divide migration and drainage capture, is permitted. At each model time step, the flow network is recalculated for the new set of elevations which arises in response to the model forcing and erosion. We set the initial boundary condition to be $z = 0$ onshore at 82 Ma. Distribution of Cretaceous marine sediments suggests that most of North America was low-lying or marine (see e.g., Fernandes et al., 2019). The offshore region is not parameterized, which does not affect our results. In summary, we start by considering the spectra of river profiles extracted from a simulated landscape generated using a simple model that includes uplift and erosion. This landscape is forced by a smoothly varying uplift rate history and eroded using a simple erosional model in which the morphodynamic Péclet number (i.e., the ratio of advective to diffusive transport) is $\gg 1$ almost everywhere that is uplifting (i.e., detachment-limited erosion prevails). Vertical features of profiles extracted from these landscape evolution models are generated by uplift forcing, by changes in drainage network topology, and by erosion rates.

Calculated landscapes as a function of time are shown in Figures 6a–6d. Unsurprisingly, these landscapes, generated with $\eta = 0$, match those produced by Fernandes et al. (2019) with a median difference (i.e., comparing elevations between the two models at the same spatiotemporal positions) of 0.04%, which arises from numerical error. Longitudinal profiles of rivers generated by this model are extracted for the trunk streams of catchments which approximate the 13 major North American catchments previously described (e.g., Colorado, Columbia, Mississippi, Nelson; Figure 1a). The shapes of the profiles approximate both observed profiles and best-fitting profiles calculated by the inverse algorithm (Figures 4 and 6e–6h, Fernandes et al., 2019). We note that, while observed river profiles extracted from digital elevation models track the water surface, profiles extracted from forward landscape models track the river bed, which is the cause of minor differences in elevation (e.g., upper reaches of “Nelson” profile in Figure 6h). In Badlands, these depressions within the channel fill with water and overflow subject to conservation of water.

The Morlet wavelet power spectra for the predicted profiles of the “Columbia,” “Colorado,” “Mississippi,” and “Nelson” rivers are shown in Figure 6i–6l. Their distance-averaged spectra from DOG wavelet analysis are shown in panels (m–p). The spectra for the other nine river profiles are shown in Supporting Information. Discussion of spectral slope trends and their similarity to observed power spectra follows in Section 4.3. Landscape evolution models were systematically tested to investigate sources of power at short wavelengths. These tests include adding quenched (i.e., temporally invariant) noise generated using the OpenSimplex algorithm, which is a modification of the gradient-based noise generation method of Perlin noise (Perlin, 1985, 2002). We use this scheme to generate distributions of noise, $\eta(x, y)$, that have known

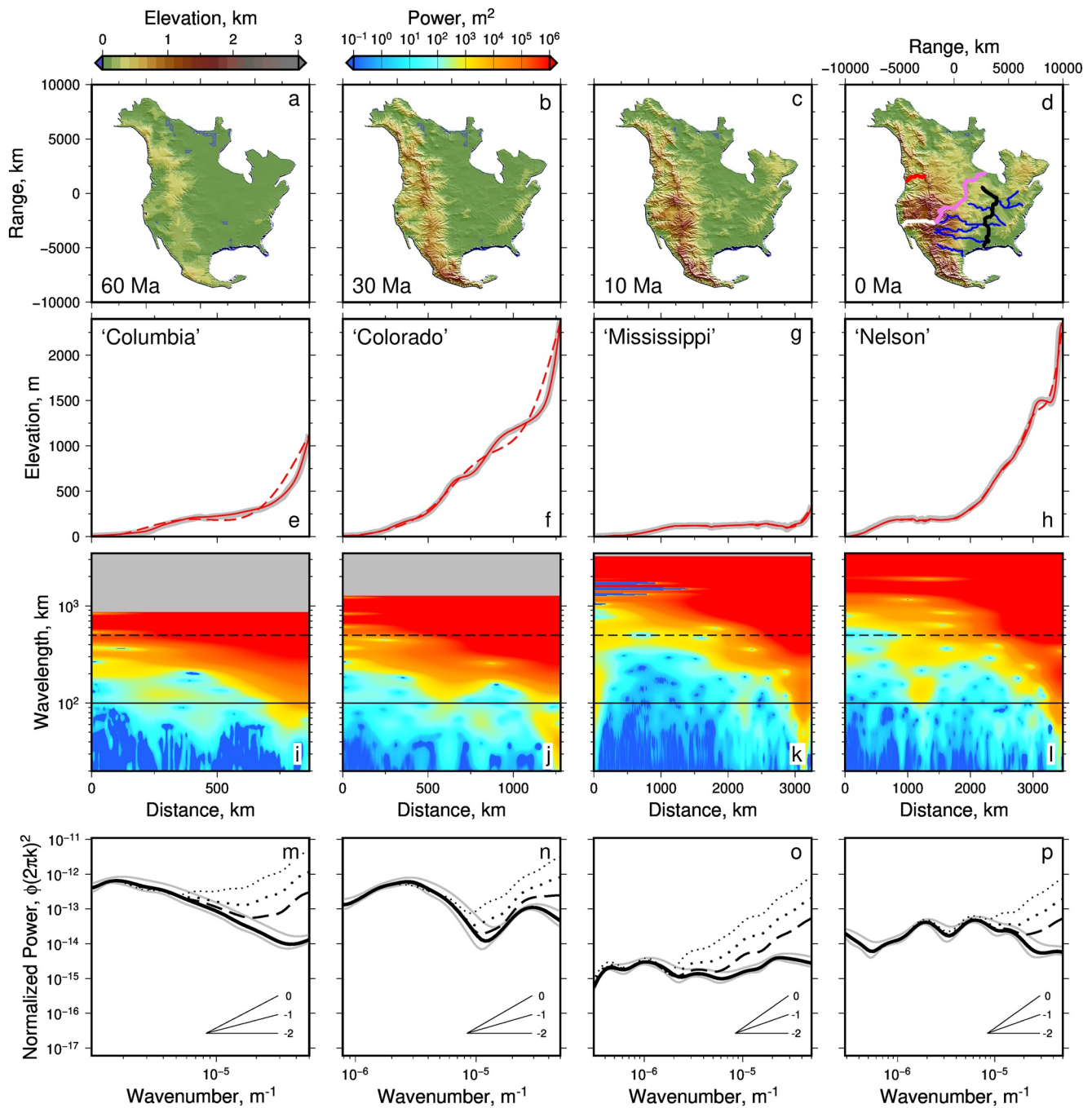


Figure 6. River profiles calculated from forward landscape simulations. (a–c) Landscape evolution generated using tectonic forcing obtained from inverse modeling (see Figure 4, Fernandes et al., 2019). (d) Calculated present-day landscape; red/white/black/pink/blue curves = principal channels of “Columbia”/“Colorado”/“Mississippi”/“Nelson”/minor rivers. (e–h) Gray curves = river profiles extracted from landscape shown in panel (d). Solid and dashed red curves = filtered inverse wavelet transforms for wavelengths ≥ 100 and ≥ 500 km (see panels i–l); transformations performed using Morlet wavelet, $\omega_s = 6$. (i–l) Power spectra for river profiles shown by gray lines in panels (e–h). Black dashed and dotted lines = wavelengths of 100 and 500 km, respectively. Gray boxes = null. (m–p) Black curves = distance-averaged derivative-of-Gaussian (DOG) ($M = 6$) power spectra of profiles shown in panels (e–h). Note normalization by $(2\pi k)^2$ so that red noise slope is horizontal. Gray curves = distance-averaged power spectra for $M = 4, 8$. Insets indicate spectral slopes: 0, -1 , -2 = white, pink, red noise; black dashed/coarse dotted/fine dotted lines = spectra for profiles with added noise where maximum amplitudes are 25/50/100 m (see Supporting Information).

power spectral slope distributions, by combining a number of discrete wavelengths of noise in a known power ratio. For example, white noise is generated where noise of each wavelength is combined with the same maximum amplitude. Red, pink, and blue noise are generated by combining noise of different wavelengths where $\eta^2 \propto k^{-2}$, $\eta^2 \propto k^{-1}$, and $\eta^2 \propto k^1$. We tested white and blue noise distributions of η , which can be regarded as representing noise of the erosional processes due to hydraulic shocks or changes in substrate. Although η can be positive or negative, we ensured $U + \eta \geq 0$. We also ran tests in which v was scaled by erodibility generated from geologic maps, L_E , or by random noise generated in an analogous way to the noise, η , previously described (supporting information, Figures S1, S8, and S9). Finally, we added quenched noise directly to river profiles extracted from the simple (i.e., no noise) landscape evolution model. Results, including power spectra, of these tests are discussed in Section 4.3, shown in Figure 6 and in the Supporting Information.

3.6. Cross-Wavelet Spectral Analysis

Here, we seek a methodology that enables the contribution that externally driven uplift makes to families of river profiles to be discriminated from other processes. We exploit cross-wavelet transforms to objectively compare different river profiles as a function of space and wave number. The cross-wavelet spectrum is calculated using

$$W^{AB} = W^A W^{B*}, \quad (8)$$

where W^A is the power spectrum of river profile a_x , and W^{B*} is the complex conjugate of the wavelet transform of river profile b_x . If both wavelet transforms are real valued, the cross-wavelet spectrum is obtained by multiplying the two transformed signals. The resultant cross-wavelet power spectrum, $|W^{AB}|$, is highest where large amplitude signals on both rivers occupy the same distance-wave number space (Grinsted et al., 2004; Roberts, 2019).

4. Results

4.1. Power Spectra of North American River Profiles

Figure 2a shows that the Columbia River has a concave-upward profile at long wavelengths with numerous knickpoints along its length. The two largest knickpoints occur at distances of ~ 900 and $\sim 1,200$ km from the mouth of the river. They are centered on the Grand Coulee and Boundary dams. The calculated power spectrum of the Columbia River shows that $>99\%$ of the power occurs at wavelengths >100 km (Figure 2b). At wavelengths <100 km, power is lower and it is determined by the positions of knickpoints. Unsurprisingly, the two dams are significant sources of power at short wavelengths. The two horizontal (solid and dashed lines at 100 and 1,000 km, respectively) show the lower bounds of the wavelet spectra used to perform inverse wavelet transforms. The resultant filtered profiles are presented in Figure 1a. The error of the inverse transform obtained using wavelengths $>1,000$ km is 4%, or 53 m in terms of error of the mean. The equivalent error for wavelengths >100 km is 0.5% or 7 m. These results combined with visual inspection of Figure 2a reinforce our assertion that most of this river profile is generated at wavelengths >100 km. Distance-averaged power spectra shown in Figures 2c–2f demonstrate the inverse power law relationship between ϕ and k . Figures 2f and 2g shows that at wavelengths $\gtrsim 100$ km, the profile broadly follows a red noise regime (i.e., $\phi \propto k^{-2}$). At shorter wavelengths, distance-averaged power spectra exhibit pink noise (i.e., $\phi \propto k^{-1}$). Spectra for 12 North American river profiles are presented in Figure 3. Similar results are obtained for different rivers, e.g., $>94\%$ of the Colorado River profile is generated at wavelengths $>1,000$ km, $>99\%$ is generated at wavelengths >100 km. The results for the Mississippi and Nelson profiles are $>1,000$ km: $>97\%$, >100 km: $>99\%$. These results show that shapes of major North American river profiles are principally generated at long wavelengths.

Most of the river profiles have distance-averaged spectra that transition from red noise at long wavelengths to pink noise at wavelengths $\lesssim 100$ km (Figure 3). The misfit between observed and calculated spectra contain well-defined minima in most cases. Trade-offs exist between calculated spectral slopes (e.g., Figure 2g), especially when observed spectra contain localized prominent peaks. A clear example of an additional peak

in distance-averaged power is shown between wave number bands 5×10^{-6} and 10^{-5} m^{-1} along the Colorado River profile. In contrast, the best-fitting two-component spectral models for the Rio Grande and Allegheny River contain a pink noise spectrum at the longest wavelength. However, a red noise spectrum at long wavelengths and a pink noise spectrum at short wavelengths fit the observed distance-averaged spectra almost equally as well, if the transition between spectra regimes occurs at a wavelength of $\sim 10 \text{ km}$ (Figures 3p and 3r).

4.2. Sources of Spectral Power

We wish to explore environmental factors that could generate observed power spectra. There are two widely accepted sources of fluvial forcing: regional uplift and bedrock erodibility. A significant constraint on the pattern and history of regional uplift of North America is the distribution of Cretaceous to Recent marine sedimentary rocks (Figures 1c and 4j, see e.g., Fernandes et al., 2019). These observations suggest that significant parts of North America have been uplifted by hundreds to thousands of meters since Cretaceous times. The results of earthquake tomographic models show that the kilometer-scale topography of western North America is not entirely supported by crustal thickness variations (e.g., Buehler & Shearer, 2016). Instead, shear wave tomography, P-to-S receiver functions, long-wavelength free-air gravity anomalies and basalt chemistry imply that the subplate mantle plays a key role in generating and maintaining regional topography (e.g., Klöcking et al., 2018; Wilson et al., 2005). Significant rivers (e.g., Columbia, Colorado, Nelson, North and South Platte, Missouri, Arkansas) flow away from the dynamically supported western North American swell (Figure 1b, Lipp & Roberts, 2021; Roberts et al., 2012).

Inverse modeling of drainage patterns indicates that the swell grew in a series of stages during Cenozoic times (Figure 4). Spectral analysis of best-fit river profiles calculated by inverse modeling shows the importance of red noise over a range of wave numbers. Calculated spectra match the long-wavelength ($>100 \text{ km}$) components of spectra generated by transforming observed river profiles (Figures 2b and 5b). However, the spectra of these best-fitting theoretical profiles underpredict power at wavelengths $\lesssim 100 \text{ km}$ (e.g., Figure 5c). Roberts et al. (2019) suggested that adding white or blue noise to power spectra can produce the observed self-similarity at wavelengths $\gtrsim 100 \text{ km}$, with a transition to pink spectral slopes at shorter wavelengths. To investigate possible sources of underpredicted spectral power at short wavelengths, we first explore the spectral content of changes in erodibility along significant river profiles (e.g., Columbia, Colorado, Nelson, Mississippi). Distance-wavelength maps of erodibility power are different to those produced by transforming river profiles generated by smoothly varying uplift rate histories (compare Figures 5b and 5e). Power spectra of erodibility spatial series have greatest power at wavelengths $<100 \text{ km}$, where spectra have a white noise distribution (Figures 5e and 5f, Supporting Information). At longer wavelengths, distance-averaged power decreases gradually, resembling blue noise.

Figure 5g presents a power spectral map generated by combining the spectra of calculated river profiles (Figure 5b) and erodibility (Figure 5e). A distance-averaged spectrum from this model is compared with the observed power spectrum of the Columbia River in Figure 5h. The black curves in this panel show the results of adding erodibility spectra scaled by factors of 10–1,000 to the best-fitting theoretical profile. Figure 5i shows the difference between power spectrum of the observed and calculated profile (i.e., Figures 3b and 5g). The scaled version of the erodibility spectra that most closely resemble spectra of the observed profile at short wavelengths indicates that changes in erodibility generate distance-averaged power of up to $\sim 10^{-2} \text{ m}^2$, which indicates that, on average, changes in erodibility generate $<1 \text{ m}$ of signal along the Columbia River. Changes in erodibility generate larger signals at a few positions along the river (i.e., yellow strips at wavelengths $<100 \text{ km}$ in Figure 5g). At these locations, power reaches up to $\sim 10^4 \text{ m}^2$ (i.e., signal amplitudes reach $\sim 100 \text{ m}$). The biggest discrepancies between observed and calculated spectra lie between ~ 500 and $1,500 \text{ km}$ distance, for wavelengths of $100\text{--}500 \text{ km}$, which coincides with the position of the two large dams (e.g., Figures 2a and 5i). Analyses of the other 11 large rivers (e.g., Colorado, Mississippi, Nelson) yield similar results (Supporting Information). This approach provides a basis for defining horizontal and vertical scales at which changes in erodibility generate changes in relief.

A remaining concern is that comparing the absolute difference in power spectra tends to imply that parts of signals with small amplitudes look similar. Figure S6 of supporting information shows the percentage difference between observed and calculated spectra. This figure suggests that the models are a high fidelity

representation of observed power spectra at long wavelengths. However, loci of short-wavelength power (e.g., knickpoints) are not well constrained. These results imply that, while it is straightforward to use erodibility to represent the average properties of river profiles at short wavelengths, precise loci of knickpoints may be more poorly constrained.

4.3. Landscape Simulations With Added Noise

Most spectral power of synthetic river profiles extracted from simple (i.e., constant value of v , no added noise, $\eta = 0$) three-dimensional landscape evolution model is concentrated at wavelengths >100 km (Figure 6). Spectra have a red noise distribution across all wavelengths such that $z^2 \propto k^{-2}$. In these cases, the inverse transforms of spectra match input signals with 5% error, even when power at wavelengths <500 km is omitted from the reconstruction (Figures 6e–6l). This result is borne out in the distance-averaged power spectra for profiles of larger rivers (e.g., Colorado, Columbia, Mississippi). Although noisy, these spectra do not exhibit significant increases or decreases in power as a function of wave number when normalized by $(2\pi k)^2$ (Figures 6m–6p, and supporting Figure S9). This result reflects the fact that power spectra of calculated river profiles are also broadly self-similar across all scales (Figures 5a–5c). These combined results suggest that the forcing which moderates landscape evolution at wavelengths $\lesssim 100$ km is absent. Since the model is only forced by the regional uplift history generated by inverse modeling of observed river profiles, the absence of pink noise suggests that tectonic forcing is also self-similar, an inference that previously been made (e.g., Flament et al., 2013; Hoggard et al., 2016; Ricard et al., 1993).

Figures 6m–6p also show spectra for river profiles that are the same as the final calculated profiles presented in Figures 6e–6h, but with noise. White noise was added to the final predicted longitudinal profiles, commensurate with the spectral power of erodibility at wavelengths $\lesssim 100$ km (Figure 5). These profiles do contain clear, systematic changes in power normalized by $(2\pi k)^2$. As wave number increases, the transition from red to pink noise is evident. This transition is more dramatic and occurs at smaller wave numbers when the amplitude of added noise is greater. Adding noise with maximum amplitudes of ≤ 100 m is enough to generate dramatic changes in power spectral slope, similar to those visible in the power spectra of observed river profiles. This result implies that processes not incorporated within the forward model parametrization generate features which are small in amplitude and wavelength in comparison to the self-similar tectonic forcing, but are nevertheless emergent at smaller scales.

An alternative approach is to add noise directly into the space-time dependent landscape evolution model through, say, η of Equation 7. This addition can also generate increased power and changes in spectral slope at short wavelengths in synthetic river profiles (see supporting information Figure S10). It is also straightforward to test the impact of noisy erosional prefactors or of erodibility scaled by the observed lithology (e.g., v , supporting Figures S9 and S11–S12), as a proxy for variable substrate strength. The results imply that adding noise provides a means to generate synthetic river profiles that are similar to observed profiles. Consistent with analyses of observed profiles, power added by noise has maximum amplitudes of ~ 100 m. Increases of power of this magnitude arise in several tests, whereby noise is added to v , so that it varies between 0 and $2 \text{ m}^{0.2} \text{ Ma}^{-1}$ (as opposed to the calibrated value of $\sim 0.99 \text{ m}^{0.2} \text{ Ma}^{-1}$) with excursions in η of $\sim 0.07 \text{ mm yr}^{-1}$ (Supporting Information). Results for tests where noise in η and in v varies through space and time did not generate significant changes in power spectra since the noise was not quenched (i.e., consistent features do not arise through time) and temporally variable random signals are likely to destructively interfere. However, we have shown that several different sources of spatially variant quenched noise can generate permanent changes in power spectral slope for river profiles generated by landscape simulation, approximating the scaling regimes observed in North American river profiles.

This approach provides a potential means of modeling landscape evolution across the scales of interest and introducing appropriately scaled structure (e.g., quenched noise as a proxy for substrate variability) that is not considered by inverse modeling of river profiles. It also provides a formal validation of the process of adding noise to generate short-wavelength signals to more closely approximate those observed in landscapes, which are not generally well replicated in simple forward models of landscape evolution subject to stream power law erosion.

4.4. Appalachian River Profiles and Spectra

Sources of power can also be investigated by comparing river profiles and environmental factors from neighboring catchments. Here, we focus on Appalachian rivers, where environmental processes are debated (Figures 7 and 8). The Appalachian orogeny occurred in Paleozoic times and the post orogenic mountain range occurs on crust that is ~50-km thick (see e.g., Buehler & Shearer, 2016). The crust is thinner beneath the coastal plain and overlain by Cenozoic sedimentary rocks (Garrity & Soller, 2009). These two physiographic provinces are separated from the Appalachian mountains by the Fall Line. This boundary runs parallel to the eastern coastline and marks a boundary of short but rapid elevation change, expressing itself in the drainage as a series of knickpoints. Present-day Appalachian topography is attributed to erosion of an ancient orogen, subplate support, the interaction of drainage patterns with lithology at the Fall Line, and to some extent glacial isostatic adjustment (e.g., Gallen et al., 2013; Reed, 1981; Rowley et al., 2013). During the Last Glacial Maximum the Laurentide Ice Sheet probably extended across the northern rivers of this region, which means that its peripheral bulge probably continued further south. Prior to this time, ice sheet melt created discharge fluctuations as far south as the Rio Grande (Wickert, 2016). Glacial isostatic adjustment has undoubtedly influenced sediment transport and incision rates of the Hudson, Delaware, Susquehanna, and Potomac rivers over the last several thousands of years (Pico et al., 2019). Here, we focus our analyses on river profiles draining the southern Appalachians.

Figure 7a shows the distribution of Cenozoic marine rock recorded across the southern Appalachians, long-wavelength free-air gravity anomalies, and six of the major rivers draining this region. Figure 7b shows these rivers superimposed upon the geologic map. Figure 7c presents river profiles, substrate, and calculated changes in erodibility. These observations are spectrally transformed and a subset are shown in Figure 8. Inverse wavelet transforms for wavelengths >100 km are presented in Figure 7c. Spectra are provided within the Supporting Information. These river profiles exhibit a similar inverse power law relationship as found elsewhere. The greatest power occurs at the longest wavelengths with evidence of a transition from red to pink noise at a wavelength of ~100 km.

Cross-wavelet analysis was carried out to determine scales and positions of dissimilarities and similarities of river profiles. Spectra were calculated using the Roanoke River profile, which drains the center of the topographic swell, for signal a_x (see Equation 8). Figures 8g and 8h show two examples of cross-wavelet power spectra for three river profiles. The Santee and James profiles are very similar to the Roanoke profile at wavelengths >100 km. At shorter wavelengths, they match well at finite positions along these different profiles. Figure 8i shows the wave number-averaged (i.e., mean) power at wavelengths >100 km along the six river profiles. Cross-wavelet power at these longer wavelengths is lower for profiles that are more distal to the Roanoke. These results imply that the long-wavelength shapes of profiles are similar at the center of the swell (i.e., in the vicinity of the Roanoke) and that they become more dissimilar toward the edges of the swell. We note that erodibility along these profiles have similar distributions to those shown for longer North American river profiles. These results imply that the bulk of shapes of Appalachian rivers are generated by regional uplift, which created shared river profile shapes at longer wavelengths. Changes in erodibility of substrate play an emergent role in moderating profile shapes at wavelengths <100 km.

4.5. Summary

Figure 9 summarizes the results of our study. Figure 9a presents spectra for the Colorado, Columbia, Mississippi, and Nelson rivers together with mean spectra for the 13 significant rivers of Figures 1 and 3. Spectra for nine additional rivers that lie between the Colorado and Mississippi and were omitted for clarity. Figure 9b shows mean spectrum, where power is multiplied by $(2\pi k)^2$. This spectrum is characterized by red noise at wavelengths ≥ 50 km and pink noise at shorter wavelengths. To investigate the sources of these signals, we examine the distance-averaged spectra of 13 synthetic rivers generated by forcing the Badlands landscape evolution model using the uplift history presented in Figure 4.

These examples were extracted at locations approximate to those of actual rivers (i.e., Arkansas, Columbia, Colorado, Cumberland, Mississippi, Missouri, Nelson, North and South Platte, Allegheny, and Kanawha tributaries of the Ohio, Rio Grande, Tennessee; Figure 6d). Synthetic river profiles are char-

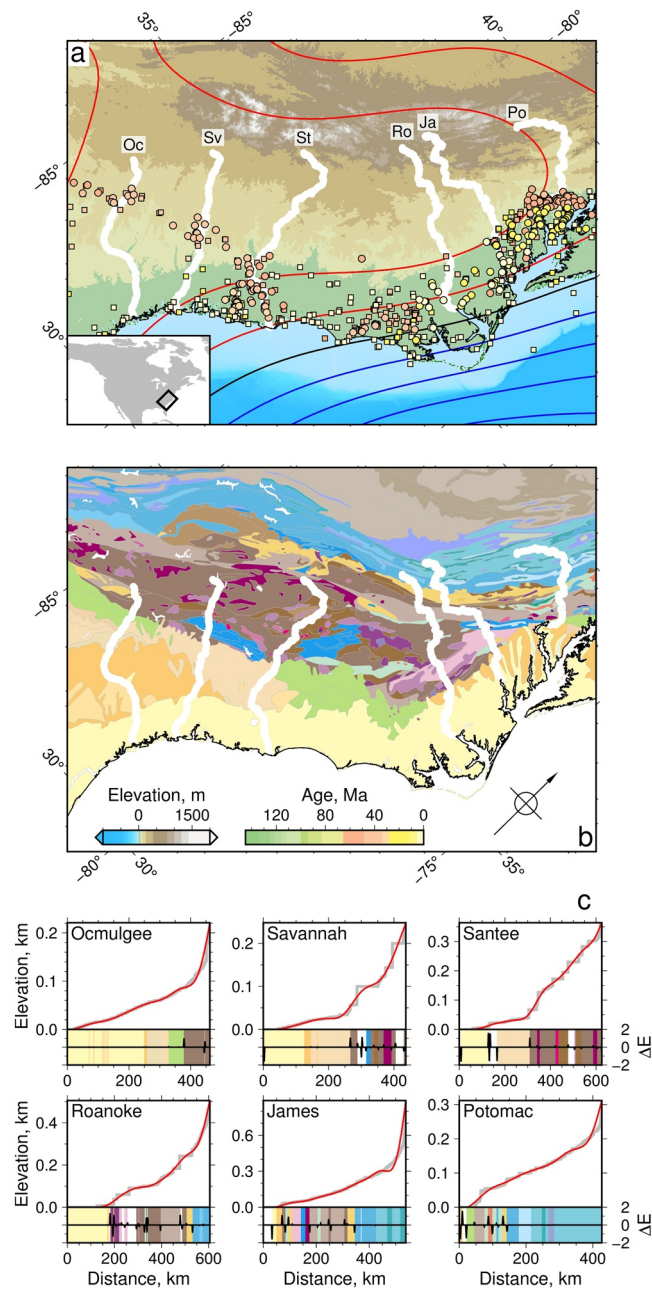
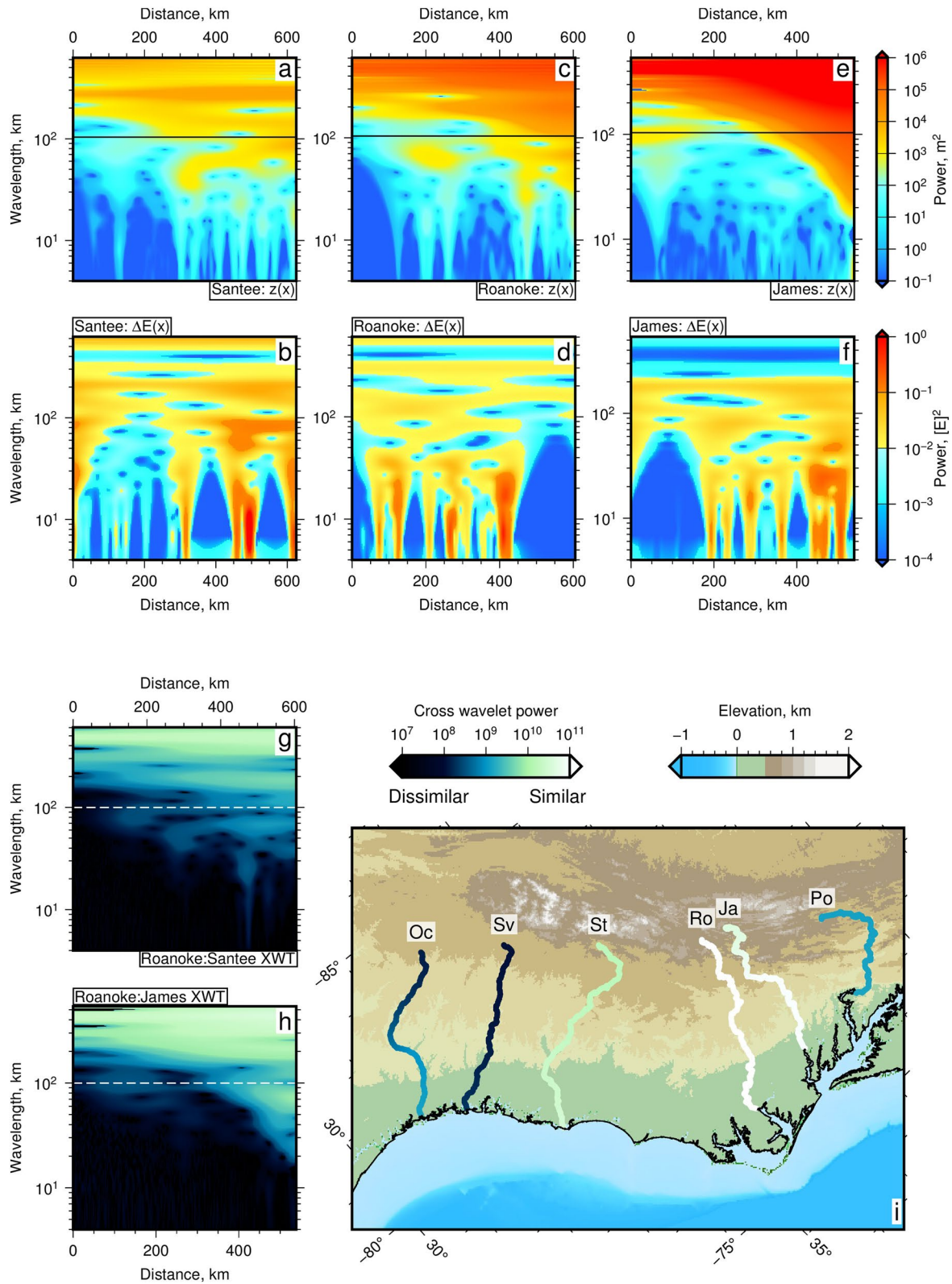


Figure 7. Appalachian drainage, lithologic, and uplift patterns. (a) Topography extracted from ETOPO1 database. Red/black/blue contours = positive/zero/negative long-wavelength (≥ 800 km) free-air gravity anomalies at intervals of 5 mGal extracted from gravity recovery and climate experiment (GRACE) database (Figure 1). Colored circles/squares = uplifted Cenozoic marine sedimentary rocks with paleobathymetric constraints from Paleobiology Database (see e.g., Fernandes et al., 2019). See panel (b) for scale bars. Labeled white curves = Ocmulgee (Oc), Savannah (Sv), Santee (St), Roanoke (Ro), James (Ja), and Potomac (Po) rivers. Inset map shows location of panel (a). (b) Geologic map of North America. White curves = major rivers. Scale bar for Cretaceous to recent rocks; brown/blue/purple = Paleozoic rocks (see Figure 1c for color scale). (c) Labeled gray lines = river profiles from panels (a) and (b); colored boxes = lithology along each profile; black spikes = change in calculated erodibility, $\Delta E(x)$, along each profile. Red lines = inverse wavelet transforms for wavelengths > 100 km (see Figure 8).

acterized by red noise (i.e., $\phi \propto k^{-2}$), which indicates self-similarity (Figure 9c). They lack the power of observed rivers at wavelengths $O(10)$ km and do not display pink noise. Second, we examine the potential contribution that lithologic heterogeneity makes to power spectra. Figure 9d shows the mean spectrum of the erodibility spatial series for these 13 rivers, which is characterized by blue noise



at wavelengths $\gtrsim 50$ km and white noise at even shorter wavelengths. Figure 9e shows the mean distance-averaged spectrum of observed rivers which once again shows that red noise transitions into pink noise at wavelengths shorter than ~ 100 km. Observed river profiles can be generated by combining long-wavelength profiles and short-wavelength changes in erodibility calculated from lithologic heterogeneity (Figures 9f and 9g).

We propose that the bulk of shapes of North American river profiles are generated at wavelengths > 100 km (Figure 9a). Inverse and forward models that are calibrated with independent geologic observations suggest the landscape is externally forced by the long-wavelength pattern of regional uplift (Figures 9c and 9f). River profiles draining the Appalachian Belt have highest cross-wavelet power (i.e., the most similar shapes) at these wavelengths (Figures 8g and 8h). At long wavelengths, $> O(10)$ km, spectra of North American rivers exhibit red (i.e., Brownian) noise (Figures 2 and 3). We note that dynamic topography generated and maintained by mantle convective processes has a similar spectrum (Hoggard et al., 2016). This similarity suggests that mantle geodynamic processes play a significant role in sculpting fluvial landscapes in space and time. The corollary is that suites of river profiles indirectly record the evolution of subplate thermal anomalies. At shorter wavelengths, river profile spectra have less power and pink noise is emergent (i.e., $\phi \propto k^{-1}$, Figures 2f and 3). Synthetic profiles forced by a combination of smoothly varying uplift histories and stream power erosion do not exhibit this short-wavelength power (Figure 9c). We suggest that power at these wavelengths is principally generated by small amplitude changes in erodibility, which have blue or white noise characteristics (Figure 9b). Erodibility appears to add < 1 m of relief to river profiles on average but can be locally significant. For example, it can generate up to ~ 100 m of relief at short wavelengths (tens of kilometers or less).

5. Conclusions

Wavelet spectral analysis is applied to selected longitudinal river profiles from North America. This technique enables us to quantify locations and scales at which shapes of river profiles are generated. Cross-wavelet spectral analysis of Appalachian river profiles is carried out to quantify similarities and discrepancies along river profiles. We investigate the origins of spectral power by transforming synthetic river profiles generated by inverse modeling of large inventories of observed river profiles as a function of uplift rate history. We transform changes in substrate erodibility and explore how its spectral content can be combined with spectra generated from synthetic river profiles forced by smooth patterns of regional uplift. We also examine how landscape simulations can be parameterized, so that they predict synthetic river profiles that are consistent with observed profiles over the scales of interest. Most of the shapes of North American river profiles can be explained as a consequence of external forcing by smoothly varying uplift rate histories and of stream power erosion. A linear version of the stream power formulation (e.g., constant erosional parameter values, zero substrate variability, invariant precipitation, discharge a function of upstream drainage area) encapsulates sufficient complexity to match observed profiles at scales > 100 km. We propose that changes in substrate erodibility can account for minor changes in river profile shapes that cannot be explained by variations of regional uplift rate. A future challenge is parameterization of landscape evolution models so that they contain appropriate scalings. Incorporation of erodibility and environmental variability is difficult to achieve deterministically since the way in which these processes change on geologic time scales is poorly understood. A pragmatic way forward is to insert environmental variability into landscape simulations by incorporating stochastic distributions that honor the spectral content of observed landscapes.

Figure 8. Elevation and erodibility spectra for selected Appalachian river profiles. (a) Power spectra for Santee River profile (Figure 7). Solid line = lower limit of filter (100 km) used to perform inverse wavelet transform (Figure 7c). (b) Wavelet power spectrum of change in erodibility, $\Delta E(x)$, along Santee River; see Figure 7c for $\Delta E(x)$ spatial series. (c and d) and (e and f) Power spectra for Roanoke and James river profiles. (g and h) Cross-wavelet power spectra between Roanoke and Santee or James river profiles; light colors = similar portions of profiles in wave number-distance space. (i) Average cross-wavelet spectra for river profiles, $z(x)$, for wavelengths > 100 km. Oc = Ocmulgee, Sv = Savannah, St = Santee, Ro = Roanoke, Ja = James, Po = Potomac. All profiles compared to Roanoke profile.

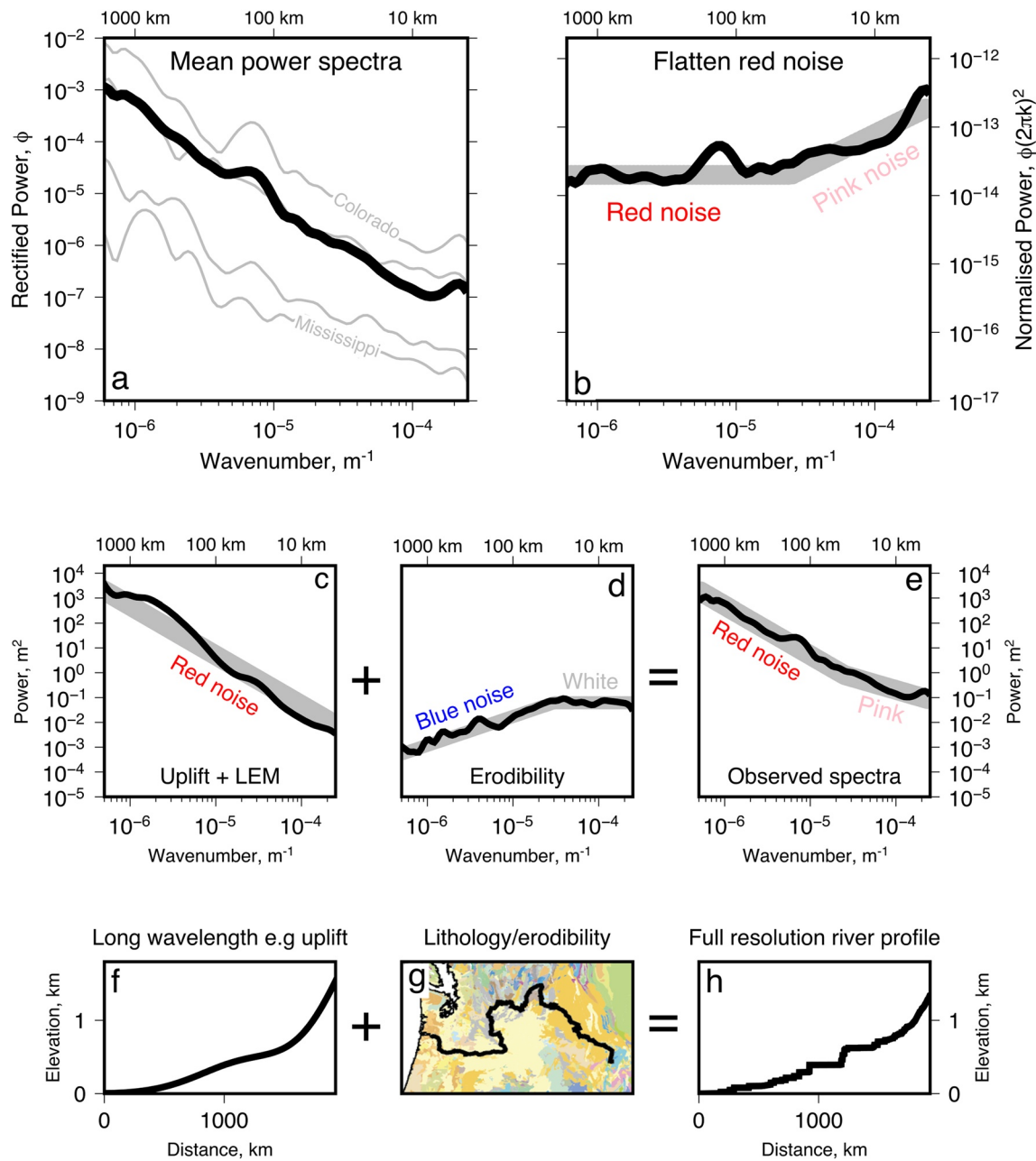


Figure 9. Principal contributions to scaling of power spectra. (a) Black curve = mean distance-averaged power spectrum for 13 North American river profiles (Figures 1–3). Labeled gray lines = spectra of Colorado, Columbia, Nelson, and Mississippi river profiles. (b) Black line = mean power spectrum from panel a multiplied by $(2\pi k)^2$. Gray band = best-fitting two-component spectral model; red and pink noise = spectral slopes -2 and -1 , respectively. (c–e) Long-wavelength and short-wavelength contributions to landscape in wave number space. (c) Mean spectrum from 13 river profiles calculated from landscape simulation (Figure 6). Solid black = rectified spectrum multiplied by 10^6 ; gray band = red noise. (d) Black line = mean spectrum from 13 erodibility profiles along observed river profiles (Figures 1 and 5). Gray lines = best-fitting two-component spectral model. (e) Black line = mean power spectrum from panel a multiplied by 10^6 . Gray band = best-fitting two-component model from panel (b). (f–h) Summary of long-wavelength and short-wavelength contributions to river profiles. (f) Black line = long-wavelength components of Columbia River profile generated by uplift and erosion. (g) Black line = planform of river superimposed upon lithologic variation (see Figure 1 for scale bar). (h) Columbia River profile.

Data Availability Statement

ASTER GDEM database can be downloaded from <https://asterweb.jpl.nasa.gov/gdem.asp>. Wavelet transforms performed using modified version of the Machine Learning Python module (<https://mlpy.sourceforge.net>). Software, example of river profile and plotting script archived at <http://doi.org/10.5281/zenodo.4013135>. Badlands algorithm can be accessed at <https://badlands.readthedocs.io>. Perlin noise generated using modified version of Noise 1.2.2 Python module (<https://pypi.org/project/noise/>).

Acknowledgments

The authors thank M. Attal, S. Gallen, A. Lipp, F. M^cNab, F. Richards, and S. Stephenson for their help. T. Salles provided an insightful review.

References

- Anderson, R. S., & Anderson, S. P. (2010). *Geomorphology: The mechanics and chemistry of landscapes*. Cambridge, UK: Cambridge University Press. <https://doi.org/10.1017/cbo9780511794827>
- Attal, M., Tucker, G., Whittaker, A., Cowie, P., & Roberts, G. P. (2008). Modeling fluvial incision and transient landscape evolution: Influence of dynamic channel adjustment. *Journal of Geophysical Research*, *113*, F03013. <https://doi.org/10.1029/2007JF000893>
- Baldwin, J. A., Whipple, K. X., & Tucker, G. E. (2003). Implications of the shear stress river incision model for the timescale of postorogenic decay of topography. *Journal of Geophysical Research*, *108*(B3), 2158. <https://doi.org/10.1029/2001JB000550>
- Batchelor, C. L., Margold, M., Krapp, M., Murton, D. K., Dalton, A. S., Gibbard, P. L., & Manica, A. (2019). The configuration of Northern Hemisphere ice sheets through the Quaternary. *Nature Communications*, *10*, 3713. <https://doi.org/10.1038/s41467-019-11601-2>
- Bell, T. H. (1975). Statistical features of sea-floor topography. *Deep Sea Research and Oceanographic Abstracts*, *22*, 883–892. [https://doi.org/10.1016/0011-7471\(75\)90090-X](https://doi.org/10.1016/0011-7471(75)90090-X)
- Birnir, B., Smith, T. R., & Merchant, G. E. (2001). The scaling of fluvial landscapes. *Computers and Geosciences*, *27*, 1189–1216. [https://doi.org/10.1016/S0098-3004\(01\)00022-X](https://doi.org/10.1016/S0098-3004(01)00022-X)
- Braun, J. (2002). Quantifying the effect of recent relief changes on age–elevation relationships. *Earth and Planetary Science Letters*, *200*(3–4), 331–343. [https://doi.org/10.1016/S0012-821X\(02\)00638-6](https://doi.org/10.1016/S0012-821X(02)00638-6)
- Braun, J., & Sambridge, M. (1997). Modelling landscape evolution on geological time scales: A new method based on irregular spatial discretization. *Basin Research*, *9*, 27–52. <https://doi.org/10.1046/j.1365-2117.1997.00030.x>
- Braun, J., & Willett, S. D. (2013). A very efficient O(n), implicit and parallel method to solve the stream power equation governing fluvial incision and landscape evolution. *Geomorphology*, *180–181*, 170–179. <https://doi.org/10.1016/j.geomorph.2012.10.008>
- Buehler, J. S., & Shearer, P. M. (2016). Uppermost mantle seismic velocity structure beneath USArray. *Journal of Geophysical Research: Solid Earth*, *122*, 436–448. <https://doi.org/10.1002/2016JB013265>
- Burke, K., & Gunnell, Y. (2008). *The African erosion surface: A continental-scale synthesis of geomorphology, tectonics, and environmental change over the past 180 million years* (p. 66). Geological Society of America. <https://doi.org/10.1130/2008.1201>
- Bursztyn, N., Pederson, J. L., Tressler, C., Mackley, R. D., & Mitchell, K. J. (2015). Rock strength along a fluvial transect of the Colorado Plateau: Quantifying a fundamental control on geomorphology. *Earth and Planetary Science Letters*, *429*, 90–100. <https://doi.org/10.1016/j.epsl.2015.07.042>
- Campforts, B., Vanacker, V., Herman, F., Vanmaercke, M., Schwanghart, W., Tenorio, G. E., et al. (2020). Parameterization of river incision models requires accounting for environmental heterogeneity: Insights from the tropical Andes. *Earth Surface Dynamics*, *8*, 447–470. <https://doi.org/10.5194/esurf-8-447-2020>
- Cloetingh, S., Ziegler, P., Beekman, F., Andriessen, P., Matenco, L., Bada, G., et al. (2005). Lithospheric memory, state of stress and rheology: Neotectonic controls on Europe's intraplate continental topography. *Quaternary Science Reviews*, *24*, 241–304. <https://doi.org/10.1016/j.quascirev.2004.06.015>
- Courant, R., Friedrichs, K., & Lewy, H. (1967). On the partial difference equations of mathematical physics. *IBM Journal of Research and Development*, *11*, 215–234. <https://doi.org/10.1147/rd.112.0215>
- Crow, R., Karlstrom, K., Darling, A., Crossey, L., Polyak, V., Granger, D., et al. (2014). Steady incision of Grand Canyon at the million year timeframe: A case for mantle-driven differential uplift. *Earth and Planetary Science Letters*, *397*, 159–173. <https://doi.org/10.1016/j.epsl.2014.04.020>
- Daubechies, I. (1990). The wavelet transform, time-frequency localization and signal analysis. *IEEE Transactions on Information Theory*, *36*, 961–1005. <https://doi.org/10.1109/18.57199>
- DiBiase, R. A., Denn, A. R., Bierman, P. R., Kirby, E., West, N., & Hidy, A. J. (2018). Stratigraphic control of landscape response to base-level fall, Young Womens Creek, Pennsylvania, USA. *Earth and Planetary Science Letters*, *504*, 163–173. <https://doi.org/10.1016/j.epsl.2018.10.005>
- Duxbury, J., Bierman, P. R., Portenga, E. W., Pavich, M. J., Southworth, S., & Freeman, S. P. H. T. (2015). Erosion rates in and around Shenandoah National Park, Virginia, determined using analysis of cosmogenic ¹⁰Be. *American Journal of Science*, *315*, 46–76. <https://doi.org/10.2475/01.2015.02>
- England, P., & Molnar, P. (1990). Surface uplift, uplift of rocks, and exhumation of rocks. *Geology*, *18*, 1173–1177. [https://doi.org/10.1130/0091-7613\(1990\)018<1173:SUUORA>2.3.CO;2](https://doi.org/10.1130/0091-7613(1990)018<1173:SUUORA>2.3.CO;2)
- Fenneman, N. M. (1928). Physiographic divisions of the United States. *Annals of the Association of American Geographers*, *18*, 261–353. <https://doi.org/10.1080/00045602809357034>
- Fernandes, V. M., Roberts, G. G., White, N., & Whittaker, A. C. (2019). Continental-scale landscape evolution: A history of North American topography. *Journal of Geophysical Research: Earth Surface*, *124*, 2689–2722. <https://doi.org/10.1029/2018JF004979>
- Flament, N., Gurnis, M., & Müller, R. D. (2013). A review of observations and models of dynamic topography. *Lithosphere*, *5*, 189–210. <https://doi.org/10.1130/L245.1>
- Gallen, S. F. (2018). Lithologic controls on landscape dynamics and aquatic species evolution in post-orogenic mountains. *Earth and Planetary Science Letters*, *493*, 150–160. <https://doi.org/10.1016/j.epsl.2018.04.029>
- Gallen, S. F., Wegmann, K. W., & Bohnenstiehl, D. R. (2013). Miocene rejuvenation of topographic relief in the southern Appalachians. *GSA Today*, *23*, 4–10. <https://doi.org/10.1130/gsatg163a.1>
- Gallen, S. F., Wegmann, K. W., Frankel, K. L., Hughes, S., Lewis, R. Q., Lyons, N., et al. (2011). Hillslope response to knickpoint migration in the Southern Appalachians: Implications for the evolution of post-orogenic landscapes. *Earth Surface Processes and Landforms*, *36*, 1254–1267. <https://doi.org/10.1002/esp.2150>

- Gao, C. (2011). Buried bedrock valleys and glacial and subglacial meltwater erosion in southern Ontario, Canada. *Canadian Journal of Earth Sciences*, 48, 801–818. <https://doi.org/10.1139/e10-104>
- Garrity, C. P., Soller, D. (2009). *Database of the geologic map of North America—adapted from the map by JC reed, Jr. and others (2005)*. U.S. Dept. of the Interior, U.S. Geological Survey. <https://doi.org/10.3133/ds424>
- Glotzbach, C. (2015). Deriving rock uplift histories from data-driven inversion of river profiles. *Geology*, 43, 467–470. <https://doi.org/10.1130/G36702.1>
- Goren, L., Fox, M., & Willett, S. D. (2014). Tectonics from fluvial topography using formal linear inversion: Theory and applications to the Inyo Mountains, California. *Journal of Geophysical Research: Earth Surface*, 119, 1651–1681. <https://doi.org/10.1002/2014JF003079>
- Grinsted, A., Moore, J. C., & Jevrejeva, S. (2004). Application of the cross wavelet transform and wavelet coherence to geophysical time series. *Nonlinear Processes in Geophysics*, 11, 561–566. <https://doi.org/10.5194/npg-11-561-2004>
- Hobley, D. E. J., Adams, J. M., Nudurupati, S. S., Hutton, E. W. H., Gasparini, N. M., Istanbuloglu, E., & Tucker, G. E. (2017). Creative computing with Landlab: An open-source toolkit for building, coupling, and exploring two-dimensional numerical models of Earth-surface dynamics. *Earth Surface Dynamics*, 5, 21–46. <https://doi.org/10.5194/esurf-5-21-2017>
- Hoggard, M. J., White, N., & Al-Attar, D. (2016). Global dynamic topography observations reveal limited influence of large-scale mantle flow. *Nature Geoscience*, 9, 456–463. <https://doi.org/10.1038/ngeo2709>
- Hoggard, M. J., Winterbourne, J., Czarnota, K., & White, N. (2017). Oceanic residual depth measurements, the plate cooling model, and global dynamic topography. *Journal of Geophysical Research: Solid Earth*, 122, 2328–2372. <https://doi.org/10.1002/2016JB013457>
- Holmes, A. (1945). *Principles of physical geology (No. 1)*. Edinburgh: Thomas Nelson and Sons Ltd. <https://doi.org/10.1080/11035894509446436>
- Houseman, G., & England, P. (1993). Crustal thickening versus lateral expulsion in the Indian-Asian continental collision. *Journal of Geophysical Research*, 98, 12233–12249. <https://doi.org/10.1029/93JB00443>
- Howard, A. D., Dietrich, W. E., & Seidl, M. A. (1994). Modeling fluvial erosion on regional to continental scales. *Journal of Geophysical Research*, 99, 13971–13986. <https://doi.org/10.1029/94JB00744>
- Japsen, P., & Chalmers, J. A. (2000). Neogene uplift and tectonics around the North Atlantic: Overview. *Global and Planetary Change*, 24, 165–173. [https://doi.org/10.1016/S0921-8181\(00\)00006-0](https://doi.org/10.1016/S0921-8181(00)00006-0)
- King, L. (1978). The geomorphology of central and southern Africa. *Biogeography and ecology of southern africa, monographiae biologicae* (pp. 1–17). https://doi.org/10.1007/978-94-009-9951-0_1
- Klöcking, M., White, N. J., MacLennan, J., McKenzie, D., & Fitton, J. G. (2018). Quantitative relationships between basalt geochemistry, shear wave velocity, and asthenospheric temperature beneath western North America. *Geochemistry, Geophysics, Geosystems*, 19, 3376–3404. <https://doi.org/10.1029/2018GC007559>
- Lague, D. (2014). The stream power river incision model: Evidence, theory and beyond. *Earth Surface Processes and Landforms*, 39, 38–61. <https://doi.org/10.1002/esp.3462>
- Lamb, M. P., & Dietrich, W. E. (2009). The persistence of waterfalls in fractured rock. *Bulletin of the Geological Society of America*, 121, 1123–1134. <https://doi.org/10.1130/B26482.1>
- Lamb, M. P., Dietrich, W. E., & Sklar, L. S. (2008). A model for fluvial bedrock incision by impacting suspended and bed load sediment. *Journal of Geophysical Research*, 113, F03025. <https://doi.org/10.1029/2007JF000915>
- Lipp, A. G., & Roberts, G. G. (2021). Scale-dependent flow directions of rivers and the importance of subplate support. *Geophysical Research Letters*, 48, e2020GL091107. <https://doi.org/10.1029/2020GL091107>
- Liu, Y., Liang, X. S., & Weisberg, R. H. (2007). Rectification of the bias in the wavelet power spectrum. *Journal of Atmospheric and Oceanic Technology*, 24, 2093–2102. <https://doi.org/10.1175/2007jtecho511.1>
- McKenzie, D. (1978). Some remarks on the development of sedimentary basins. *Earth and Planetary Science Letters*, 40, 25–32. [https://doi.org/10.1016/0012-821x\(78\)90071-7](https://doi.org/10.1016/0012-821x(78)90071-7)
- Moosdorf, N., Cohen, S., & von Hagke, C. (2018). A global erodibility index to represent sediment production potential of different rock types. *Applied Geography*, 101, 36–44. <https://doi.org/10.1016/j.apgeog.2018.10.010>
- Paul, J. D., Roberts, G. G., & White, N. (2014). The African landscape through space and time. *Tectonics*, 33, 898–935. <https://doi.org/10.1002/2013TC003479>
- Pelletier, J. D. (1999). Self-organization and scaling relationships of evolving river networks. *Journal of Geophysical Research*, 104, 7359–7375. <https://doi.org/10.1029/1998JB900110>
- Perlin, K. (1985). An image synthesizer. *ACM SIGGRAPH Computer Graphics*, 19, 287–296. <https://doi.org/10.1145/325165.325247>
- Perlin, K. (2002). Improving noise. *ACM Transactions on Graphics*, 21(3), 681–682. <https://doi.org/10.1145/566654.566636>
- Perron, J. T., Kirchner, J. W., & Dietrich, W. E. (2008). Spectral signatures of characteristic spatial scales and nonfractal structure in landscapes. *Journal of Geophysical Research*, 113, F04003. <https://doi.org/10.1029/2007JF000866>
- Pico, T., Mitrovica, J. X., Perron, J. T., Ferrier, K. L., & Braun, J. (2019). Influence of glacial isostatic adjustment on river evolution along the U.S. mid-Atlantic coast. *Earth and Planetary Science Letters*, 522, 176–185. <https://doi.org/10.1016/j.epsl.2019.06.026>
- Pritchard, D., Roberts, G., White, N., & Richardson, C. (2009). Uplift histories from river profiles. *Geophysical Research Letters*, 36, L24301. <https://doi.org/10.1029/2009GL040928>
- Reed, J. C. Jr. (1981). Disequilibrium profile of the Potomac River near Washington, D.C.: A result of lowered base level or quaternary tectonics along the fall line? *Geology*, 9, 445–450. [https://doi.org/10.1130/0091-7613\(1981\)9<445:dpotpr>2.0.co;2](https://doi.org/10.1130/0091-7613(1981)9<445:dpotpr>2.0.co;2)
- Ricard, Y., Richards, M., Lithgow-Bertelloni, C., & Le Stunff, Y. (1993). A geodynamic model of mantle density heterogeneity. *Journal of Geophysical Research*, 98, 21895–21909. <https://doi.org/10.1029/93JB02216>
- Roberts, G. G. (2019). Scales of similarity and disparity between drainage networks. *Geophysical Research Letters*, 46, 3781–3790. <https://doi.org/10.1029/2019GL082446>
- Roberts, G. G., & White, N. (2010). Estimating uplift rate histories from river profiles using African examples. *Journal of Geophysical Research*, 115, B02406. <https://doi.org/10.1029/2009JB006692>
- Roberts, G. G., White, N., & Lodhia, B. H. (2019). The generation and scaling of longitudinal river profiles. *Journal of Geophysical Research: Earth Surface*, 124, 137–153. <https://doi.org/10.1029/2018JF004796>
- Roberts, G. G., White, N., Martin-Brandis, G., & Crosby, A. (2012). An uplift history of the Colorado Plateau and its surroundings from inverse modeling of longitudinal river profiles. *Tectonics*, 31, TC4022. <https://doi.org/10.1029/2012TC003107>
- Rosenbloom, N. A., & Anderson, R. S. (1994). Hillslope and channel evolution in a marine terraced landscape, Santa Cruz, California. *Journal of Geophysical Research*, 99, 14013–14029. <https://doi.org/10.1029/94JB00048>
- Rowley, D. B., Forte, A. M., Moucha, R., Mitrovica, J. X., Simmons, N. A., & Grand, S. P. (2013). Dynamic topography change of the eastern United States since 3 million years ago. *Science*, 340, 1560–1563. <https://doi.org/10.1126/science.1229180>

- Rudge, J. F., Roberts, G. G., White, N. J., & Richardson, C. N. (2015). Uplift histories of Africa and Australia from linear inverse modeling of drainage inventories. *Journal of Geophysical Research: Earth Surface*, *120*, 894–914. <https://doi.org/10.1002/2014JF003297>
- Salles, T. (2016). Badlands: A parallel basin and landscape dynamics model. *SoftwareX*, *5*, 195–202. <https://doi.org/10.1016/j.softx.2016.08.005>
- Salles, T., Flament, N., & Müller, D. (2017). Influence of mantle flow on the drainage of eastern Australia since the Jurassic Period. *Geochemistry, Geophysics, Geosystems*, *18*, 280–305. <https://doi.org/10.1002/2016GC006617>
- Schoenbohm, L. M., Whipple, K. X., Burchfiel, B. C., & Chen, L. (2004). Geomorphic constraints on surface uplift, exhumation, and plateau growth in the Red River region, Yunnan Province, China. *Bulletin of the Geological Society of America*, *116*, 895–909. <https://doi.org/10.1130/B25364.1>
- Singh, A., Lanzoni, S., Wilcock, P. R., & Foufoula-Georgiou, E. (2011). Multiscale statistical characterization of migrating bed forms in gravel and sand bed rivers. *Water Resources Research*, *47*, W12526. <https://doi.org/10.1029/2010WR010122>
- Sklar, L. S., & Dietrich, W. E. (2001). Sediment and rock strength controls on river incision into bedrock. *Geology*, *29*, 1087–1090. [https://doi.org/10.1130/0091-7613\(2001\)029<1087:SARSCO>2.0.CO](https://doi.org/10.1130/0091-7613(2001)029<1087:SARSCO>2.0.CO)
- Smith, T. R., & Bretherton, F. P. (1972). Stability and the conservation of mass in drainage basin evolution. *Water Resources Research*, *8*, 1506–1529. <https://doi.org/10.1029/WR008i006p01506>
- Spotila, J. A., Moskey, K. A., & Prince, P. S. (2015). Geologic controls on bedrock channel width in large, slowly-eroding catchments: Case study of the New River in eastern North America. *Geomorphology*, *230*, 51–63. <https://doi.org/10.1016/j.geomorph.2014.11.004>
- Stucky de Quay, G., Roberts, G. G., Rood, D. H., & Fernandes, V. M. (2019). Holocene uplift and rapid fluvial erosion of Iceland: A record of post-glacial landscape evolution. *Earth and Planetary Science Letters*, *505*, 118–130. <https://doi.org/10.1016/j.epsl.2018.10.026>
- Tachikawa, T., Kaku, M., Iwasaki, A., Gesch, D., Oimoen, M., & Zhang, Z., et al. (2011). *ASTER global digital elevation model version 2: Summary of validation results: Report to the ASTER GDEM validation team* (p. 27). NASA. <https://doi.org/10.1109/igarss.2011.6050017>
- Tapley, B., Ries, J., Bettadpur, S., Chambers, D., Cheng, M., Condi, F., & Wang, F. (2005). GGM02: An improved Earth gravity field model from GRACE. *Journal of Geodesy*, *79*, 467–478. <https://doi.org/10.1007/s00190-005-0480-z>
- Tarboton, D. G. (1997). A new method for the determination of flow directions and upslope areas in grid digital elevation models. *Water Resources Research*, *33*, 309–319. <https://doi.org/10.1029/96WR03137>
- Torrence, C., & Compo, G. P. (1998). A practical guide to wavelet analysis. *Bulletin of the American Meteorological Society*, *79*, 61–78. [https://doi.org/10.1175/1520-0477\(1998\)079<0061:apgtwa>2.0.co;2](https://doi.org/10.1175/1520-0477(1998)079<0061:apgtwa>2.0.co;2)
- Tucker, G. E., & Bras, R. L. (1998). Hillslope processes, drainage density, and landscape morphology. *Water Resources Research*, *34*, 2751–2764. <https://doi.org/10.1029/98WR01474>
- Turowski, J. M., Lague, D., & Hovius, N. (2007). Cover effect in bedrock abrasion: A new derivation and its implications for the modeling of bedrock channel morphology. *Journal of Geophysical Research*, *112*, F04006. <https://doi.org/10.1029/2006JF000697>
- Whipple, K. X., & Tucker, G. E. (1999). Dynamics of the stream-power river incision model: Implications for height limits of mountain ranges, landscape response timescales, and research needs. *Journal of Geophysical Research*, *104*, 17661–17674. <https://doi.org/10.1029/1999JB900120>
- Whipple, K. X., & Tucker, G. E. (2002). Implications of sediment-flux-dependent river incision models for landscape evolution. *Journal of Geophysical Research*, *107*(B2), 2039. <https://doi.org/10.1029/2000JB000044>
- Whittaker, A. C., Attal, M., Cowie, P. A., Tucker, G. E., & Roberts, G. (2008). Decoding temporal and spatial patterns of fault uplift using transient river long profiles. *Geomorphology*, *100*, 506–526. <https://doi.org/10.1016/j.geomorph.2008.01.018>
- Whittaker, A. C., & Boulton, S. J. (2012). Tectonic and climatic controls on knickpoint retreat rates and landscape response times. *Journal of Geophysical Research*, *117*, F02024. <https://doi.org/10.1029/2011JF002157>
- Whittaker, A. C., Cowie, P. A., Attal, M., Tucker, G. E., & Roberts, G. P. (2007). Contrasting transient and steady-state rivers crossing active normal faults: New field observations from the Central Apennines, Italy. *Basin Research*, *19*, 529–556. <https://doi.org/10.1111/j.1365-2117.2007.00337.x>
- Wickert, A. D. (2016). Reconstruction of North American drainage basins and river discharge since the last glacial maximum. *Earth Surface Dynamics*, *4*, 831–869. <https://doi.org/10.5194/esurf-4-831-2016>
- Willett, S. D., McCoy, S. W., Perron, J. T., Goren, L., & Chen, C.-Y. (2014). Dynamic reorganization of river basins. *Science*, *343*, 1248765. <https://doi.org/10.1126/science.1248765>
- Wilson, D., Aster, R., Ni, J., Grand, S., West, M., Gao, W., & Semken, S. (2005). Imaging the seismic structure of the crust and upper mantle beneath the great plains, Rio Grande Rift, and Colorado Plateau using receiver functions. *Journal of Geophysical Research*, *110*, B05306. <https://doi.org/10.1029/2004JB003492>
- Yanites, B. J., Becker, J. K., Madritsch, H., Schnellmann, M., & Ehlers, T. A. (2017). Lithologic effects on landscape response to base level changes: A modeling study in the context of the eastern jura mountains, Switzerland. *Journal of Geophysical Research: Earth Surface*, *122*, 2196–2222. <https://doi.org/10.1002/2016JF004101>
- Zondervan, J. R., Whittaker, A. C., Bell, R. E., Watkins, S. E., Brooke, S. A. S., & Hann, M. G. (2020). New constraints on bedrock erodibility and landscape response times upstream of an active fault. *Geomorphology*, *351*, 106937. <https://doi.org/10.1016/j.geomorph.2019.106937>